



NAVAL POSTGRADUATE SCHOOL

MONTEREY, CALIFORNIA

THESIS

**FREE VIBRATION RESPONSE COMPARISON OF
COMPOSITE BEAMS WITH FLUID STRUCTURE
INTERACTION**

by

Eric M. Priest

September 2012

Thesis Co-Advisors:

Young W. Kwon

Joshua H. Gordis

Second Reader

Jarema M. Didoszak

Approved for public release; distribution is unlimited.

THIS PAGE INTENTIONALLY LEFT BLANK

REPORT DOCUMENTATION PAGE			<i>Form Approved OMB No. 0704-0188</i>	
Public reporting burden for this collection of information is estimated to average 1 hour per response, including the time for reviewing instruction, searching existing data sources, gathering and maintaining the data needed, and completing and reviewing the collection of information. Send comments regarding this burden estimate or any other aspect of this collection of information, including suggestions for reducing this burden, to Washington headquarters Services, Directorate for Information Operations and Reports, 1215 Jefferson Davis Highway, Suite 1204, Arlington, VA 22202-4302, and to the Office of Management and Budget, Paperwork Reduction Project (0704-0188) Washington DC 20503.				
1. AGENCY USE ONLY (Leave blank)		2. REPORT DATE September 2012	3. REPORT TYPE AND DATES COVERED Master's Thesis	
4. TITLE AND SUBTITLE Free Vibration Response Comparison of Composite Beams with Fluid Structure Interaction			5. FUNDING NUMBERS	
6. AUTHOR(S) Eric M. Priest				
7. PERFORMING ORGANIZATION NAME(S) AND ADDRESS(ES) Naval Postgraduate School Monterey, CA 93943-5000			8. PERFORMING ORGANIZATION REPORT NUMBER	
9. SPONSORING /MONITORING AGENCY NAME(S) AND ADDRESS(ES) N/A			10. SPONSORING/MONITORING AGENCY REPORT NUMBER	
11. SUPPLEMENTARY NOTES The views expressed in this thesis are those of the author and do not reflect the official policy or position of the Department of Defense or the U.S. Government. IRB Protocol number ____N/A____.				
12a. DISTRIBUTION / AVAILABILITY STATEMENT Approved for public release; distribution is unlimited.			12b. DISTRIBUTION CODE A	
13. ABSTRACT (maximum 200 words) <p>The analysis of the dynamic response of a vibrating structure in contact with a fluid medium can be interpreted as an added mass effect known as the Fluid Structure Interaction (FSI) problem. This effect is critical in the study of composites for marine applications since the densities of the composites and water are relatively close to one another.</p> <p>In this study, experimental testing was conducted to compare the free vibration response of composite beams in air with those in FSI immersed in water. Composite beams with six layers of non-biased, plain weave, 6 oz E-glass were used with two different layer orientations and boundary conditions. Five samples were layered at the 0 and 90 degree orientations and five samples were layered at the plus and minus 45 degree orientation. The Digital Image Correlation (DIC) technique was used to test each of the ten samples in a cantilever boundary condition with an initial displacement to induce a free vibration response both in air and immerse in water. A High Speed Camera (HSC) was also used to gain further frequency information during each of these tests.</p> <p>A second set of two composite beams were constructed with 16 layers at both of the described orientations. These were instrumented with accelerometers to conduct a modal analysis from an impact hammer test. These tests were conducted with the beams in a free-free boundary condition while in air and immersed in water. Prior to conducting these tests, an aluminum beam was tested with the same conditions to verify the waterproofing of the accelerometers and to ensure valid data was collected. The findings of this study will provide a better understanding for the use of composite materials in marine applications where various excitations can occur.</p>				
14. SUBJECT TERMS Composite, Mode Shape, Fluid Structure Interaction, Digital Image Correlation, Impact Hammer Test			15. NUMBER OF PAGES 95	
			16. PRICE CODE	
17. SECURITY CLASSIFICATION OF REPORT Unclassified	18. SECURITY CLASSIFICATION OF THIS PAGE Unclassified	19. SECURITY CLASSIFICATION OF ABSTRACT Unclassified	20. LIMITATION OF ABSTRACT UU	

THIS PAGE INTENTIONALLY LEFT BLANK

Approved for public release; distribution is unlimited.

**FREE VIBRATION RESPONSE COMPARISON OF COMPOSITE BEAMS
WITH FLUID STRUCTURE INTERACTION**

Eric M. Priest
Lieutenant, United States Navy
B.A., Georgia State University, 2007

Submitted in partial fulfillment of the
requirements for the degree of

MASTER OF SCIENCE IN MECHANICAL ENGINEERING

from the

**NAVAL POSTGRADUATE SCHOOL
September 2012**

Author: Eric M. Priest

Approved by: Young W. Kwon
Thesis Co-Advisor

Joshua H. Gordis
Thesis Co-Advisor

Jarema M. Didoszak
Second Reader

Knox T. Millsaps
Chair, Department of Mechanical and Aerospace Engineering

THIS PAGE INTENTIONALLY LEFT BLANK

ABSTRACT

The analysis of the dynamic response of a vibrating structure in contact with a fluid medium can be interpreted as an added mass effect known as the Fluid Structure Interaction (FSI) problem. This effect is critical in the study of composites for marine applications since the densities of the composites and water are relatively close to one another.

In this study, experimental testing was conducted to compare the free vibration response of composite beams in air with those in FSI immersed in water. Composite beams with six layers of non-biased, plain weave, 6 oz E-glass were used with two different layer orientations and boundary conditions. Five samples were layered at the 0 and 90 degree orientations and five samples were layered at the plus and minus 45 degree orientation. The Digital Image Correlation (DIC) technique was used to test each of the ten samples in a cantilever boundary condition with an initial displacement to induce a free vibration response both in air and immerse in water. A High Speed Camera (HSC) was also used to gain further frequency information during each of these tests.

A second set of two composite beams were constructed with 16 layers at both of the described orientations. These were instrumented with accelerometers to conduct a modal analysis from an impact hammer test. These tests were conducted with the beams in a free-free boundary condition while in air and immersed in water. Prior to conducting these tests, an aluminum beam was tested with the same conditions to verify the waterproofing of the accelerometers and to ensure valid data was collected. The findings of this study will provide a better understanding for the use of composite materials in marine applications where various excitations can occur.

THIS PAGE INTENTIONALLY LEFT BLANK

TABLE OF CONTENTS

I.	INTRODUCTION.....	1
A.	COMPOSITE APPLICABILITY	1
B.	OBJECTIVE	2
II.	LITERATURE REVIEW	3
A.	COMPOSITE MAKE-UP	3
B.	HISTORICAL PERSPECTIVE	3
C.	FSI OF COMPOSITES	3
III.	EXPERIMENTAL TECHNIQUES	5
A.	DIGITAL IMAGE CORRELATION	5
1.	Theoretical Background	5
2.	Mathematical Background	6
3.	Specimen Preparation	8
B.	IMPACT HAMMER TEST	10
C.	MODAL ANALYSIS	11
1.	Time Analysis	11
2.	Frequency Analysis	12
IV.	TEST EQUIPMENT	13
A.	WATER TANK AND TESTING APPARATUS	13
B.	DIC SETUP	15
1.	Special Considerations for Testing in Water.....	16
a.	<i>Magnification of Composite Beam.....</i>	16
b.	<i>Light Refraction and Reflection</i>	16
C.	IMPACT HAMMER SETUP	18
D.	COMPOSITE SELECTION.....	19
1.	Overview	19
2.	DIC Test Composite Samples	20
3.	Impact Hammer Test Composite Samples	22
V.	TEST CONDITIONS	23
A.	OVERVIEW	23
B.	TEST SAMPLE ENVIRONMENTS	23
1.	In Air	23
2.	Submerged in Water	23
C.	TEST PROCEDURES.....	24
1.	Preliminary Calculations.....	24
a.	<i>Material Properties of Composite Samples</i>	24
b.	<i>Theoretical Natural Frequency of the Cantilever Beam</i>	25
c.	<i>Theoretical Natural Frequency of the Free-Free Beam</i>	27
2.	DIC Test Procedure	27
3.	Impact Hammer Test Procedure	29
VI.	RESULTS AND ANALYSIS	35

A.	DIC TEST	35
1.	Validation between Test Environments	35
2.	Experimental Natural Frequency of Cantilever Beam.....	37
3.	Free Vibration Response	41
B.	IMPACT HAMMER TEST	48
1.	Experimental Natural Frequency of the Free-Free Beam	48
2.	Mode Shape Comparison of the Composite Beam.....	51
VII.	CONCLUSIONS AND RECOMENDATIONS	57
APPENDIX A:	ACCELEROMETER PLACEMENTS	59
APPENDIX B:	FREE VIBRATION RESPONSE IN AIR PLOTS.....	61
APPENDIX C:	FREE VIBRATION RESPONSE IN WATER PLOTS	67
	LIST OF REFERENCES.....	73
	INITIAL DISTRIBUTION LIST	75

LIST OF FIGURES

Figure 1.	Typical stereoscopic setup.	5
Figure 2.	Subset of pixels before and after deformation. The speckle pattern has moved one pixel to the right and one pixel up. After [12].	6
Figure 3.	Graphical representation of the transformation between coordinates.	7
Figure 4.	Optimization of pixel gray scale values.	8
Figure 5.	Example representation of speckle size per pixel.	9
Figure 6.	Typical impact hammer test setup.	10
Figure 7.	Image of water tank.	13
Figure 8.	Image of cantilever testing apparatus.	14
Figure 9.	Initial DIC set up with spacing dimensions.	15
Figure 10.	Operational DIC set up.	17
Figure 11.	Image of impact hammer test setup.	19
Figure 12.	Customized speckle patterns. (a) Coarse speckle pattern. (b) Fine speckle pattern.	21
Figure 13.	Image of fabricated composite samples for DIC tests. (a) $0^{\circ}/90^{\circ}$ orientation. (b) $\pm 45^{\circ}$ orientation.	21
Figure 14.	Mode 1 of free-free aluminum beam struck by impact hammer only.	30
Figure 15.	Mode 2 of free-free aluminum beam struck by impact hammer only.	31
Figure 16.	Mode 3 of free-free aluminum beam struck by impact hammer only.	31
Figure 17.	Mode 1 of free-free aluminum beam struck by impact hammer with the steel rod.	32
Figure 18.	Mode 2 of free-free aluminum beam struck by impact hammer with the steel rod.	32
Figure 19.	Mode 3 of free-free aluminum beam struck by impact hammer with the steel rod.	33
Figure 20.	Typical moiré pattern on representative sample with fine speckle pattern.	35
Figure 21.	Displacement of composite beam in air and water environments.	36
Figure 22.	Point index line for measuring displacement along the centerline of the beam with 100 evenly spaced points.	37
Figure 23.	Determination of the period of oscillation using HSC images. (a) First free vibration peak at 0.2228 seconds. (b) Second free vibration peak at 0.2982 seconds.	37
Figure 24.	Representative sample of tip displacement as a function of time for the determination of damping.	38
Figure 25.	Fundamental frequency distribution for each cantilever beam in air environment with theoretical frequencies.	40
Figure 26.	Fundamental frequency distribution for each cantilever beam in water environment.	40
Figure 27.	Theoretical displacement configuration of Modes I, II, and III for a cantilever beam under free vibration.	42
Figure 28.	Free vibration response shape in air at various times for Sample V of $0^{\circ}/90^{\circ}$ orientation	43

Figure 29.	Free vibration response shape in water at various times for Sample V of $0^\circ/90^\circ$ orientation.	43
Figure 30.	Free vibration response shape in air at various times for Sample III of $\pm 45^\circ$ orientation.	44
Figure 31.	Free vibration response shape in water at various times for Sample III of $\pm 45^\circ$ orientation.	44
Figure 32.	Three-dimensional representation of the reference image used for correlation in air for Sample V of $0^\circ/90^\circ$ orientation.	46
Figure 33.	Three-dimensional representation of the reference image used for correlation in water for Sample V of $0^\circ/90^\circ$ orientation.	46
Figure 34.	Three-dimensional representation of the free vibration response shape at 6000 ms after the initial displacement in air for Sample V of $0^\circ/90^\circ$ orientation.	47
Figure 35.	Three-dimensional representation of the free vibration response shape at 2400 ms after initial displacement in water for Sample V of $0^\circ/90^\circ$	47
Figure 36.	Contour plot overlay of displacements along the length of the cantilever beam in water at 2400 ms after initial displacement for Sample V of $0^\circ/90^\circ$ orientation.	48
Figure 37.	Frequency distribution for Modes I, II, and III of free-free composite beam of $0^\circ/90^\circ$ orientation beams in air and water environments.	50
Figure 38.	Frequency distribution for Modes I, II, and III of free-free aluminum beam in air and water environment with theoretical frequencies.	50
Figure 39.	Theoretical mode shapes for Mode I, II, and III of a free-free beam.	52
Figure 40.	Mode I of free-free composite beam of $0^\circ/90^\circ$ orientation in air.	52
Figure 41.	Mode II of free-free composite beam of $0^\circ/90^\circ$ orientation in air.	53
Figure 42.	Mode III of free-free composite beam of $0^\circ/90^\circ$ orientation in air.	53
Figure 43.	Mode I of free-free composite beam of $0^\circ/90^\circ$ orientation in water.	54
Figure 44.	Mode II of free-free composite beam of $0^\circ/90^\circ$ orientation in water.	54
Figure 45.	Mode III of free-free composite beam of $0^\circ/90^\circ$ orientation in water.	55
Figure 46.	Composite beam with accelerometer placements.	59
Figure 47.	Free vibration response shape in air at various times for Sample I of $0^\circ/90^\circ$ orientation.	61
Figure 48.	Free vibration response shape in air at various times for Sample II of $0^\circ/90^\circ$ orientation.	62
Figure 49.	Free vibration response shape in air at various times for Sample III of $0^\circ/90^\circ$ orientation.	62
Figure 50.	Free vibration response shape in air at various times for Sample IV of $0^\circ/90^\circ$ orientation.	63
Figure 51.	Free vibration response shape in air at various times for Sample V of $0^\circ/90^\circ$ orientation.	63
Figure 52.	Free vibration response shape in air at various times for Sample I of $\pm 45^\circ$ orientation.	64
Figure 53.	Free vibration response shape in air at various times for Sample II of $\pm 45^\circ$ orientation.	64

Figure 54.	Free vibration response shape in air at various times for Sample III of $\pm 45^\circ$ orientation.	65
Figure 55.	Free vibration response shape in air at various times for Sample IV of $\pm 45^\circ$ orientation.	65
Figure 56.	Free vibration response shape in air at various times for Sample V of $\pm 45^\circ$ orientation.	66
Figure 57.	Free vibration response shape in water at various times for Sample I of $0^\circ/90^\circ$ orientation.	67
Figure 58.	Free vibration response shape in water at various times for Sample II of $0^\circ/90^\circ$ orientation.	67
Figure 59.	Free vibration response shape in water at various times for Sample III of $0^\circ/90^\circ$ orientation.	68
Figure 60.	Free vibration response shape in water at various times for Sample IV of $0^\circ/90^\circ$ orientation.	68
Figure 61.	Free vibration response shape in water at various times for Sample V of $0^\circ/90^\circ$ orientation.	69
Figure 62.	Free vibration response shape in water at various times for Sample I of $\pm 45^\circ$ orientation.	69
Figure 63.	Free vibration response shape in water at various times for Sample II of $\pm 45^\circ$ orientation.	70
Figure 64.	Free vibration response shape in water at various times for Sample III of $\pm 45^\circ$ orientation.	70
Figure 65.	Free vibration response shape in water at various times for Sample IV of $\pm 45^\circ$ orientation.	71
Figure 66.	Free vibration response shape in water at various times for Sample V of $\pm 45^\circ$ orientation.	71

THIS PAGE INTENTIONALLY LEFT BLANK

LIST OF TABLES

Table 1.	Associated Strength Properties of Derakane 510A-40 Epoxy Vinyl Ester Resin. After [23]	20
Table 2.	Overview of composite sample dimensions and orientation.	20
Table 3.	Measured bending stiffness of each beam sequence.....	24
Table 4.	Measured density of each beam sequence.	25
Table 5.	Values for $\beta_n L$ for the first three modes of a cantilever beam.....	26
Table 6.	Values for $\beta_n L$ for the first four modes of a free-free beam.....	27
Table 7.	Natural frequencies for Modes I, II, and III for each method for free-free beam aluminum beam in air.....	33
Table 8.	Theoretical and experimental fundamental frequencies of each cantilever beam in air.....	39
Table 9.	Theoretical and experimental fundamental frequencies of each cantilever beam in water.	39
Table 10.	Theoretical and experimental natural frequencies of the free-free composite beam of $0^\circ/90^\circ$ orientation and aluminum beam in air.	49
Table 11.	Experimental natural frequencies of the free-free composite beam of $0^\circ/90^\circ$ orientation and aluminum beam in water.....	49

THIS PAGE INTENTIONALLY LEFT BLANK

LIST OF ACRONYMS AND ABBREVIATIONS

CCD	Charge Couple Device
DIC	Digital Image Correlation
DSA	Digital Signal Analyzer
FSI	Fluid Structure Interaction
HSC	High Speed Camera
NAVMI	Non-dimensionalized Added Virtual Mass Incremental
VARTM	Vacuum-Assisted Resin Transfer Molding

THIS PAGE INTENTIONALLY LEFT BLANK

ACKNOWLEDGMENTS

First and foremost, I would like to thank God for always guiding me and never failing me. I would also like to thank my beautiful wife and children for their unyielding support and encouragement throughout my time at the Naval Postgraduate School.

I would to express my sincere appreciation to the following people, each one of whom has been vital in the successful completion of my thesis:

Dr. Young Kwon, for his mentorship, guidance, and advice throughout this process. His knowledge and expertise, coupled with his willingness to always be available were vital to the completion of this work.

Dr. Joshua Gordis and Wenschel Lan, for their assistance in the operation and troubleshooting of test equipment which saved my many more hours of work and frustration.

Without the support of each one of these people, none of this would have been possible. Thank you all!

THIS PAGE INTENTIONALLY LEFT BLANK

I. INTRODUCTION

A. COMPOSITE APPLICABILITY

Though composites have been around for nearly 30 years, only recently has there been an increase in its use for marine applications and shipbuilding. The reason for this is threefold. The strength to weight ratio of composites is ideal for creating lightweight, high-strength boats and ships. By weight, a composites strength and stiffness is on the same order as aluminum and steel but is much lighter in comparison. This makes the craft much faster through the water and more fuel-efficient than its steel counterparts. Additionally, composites are less expensive over its lifespan than metals used in the majority of shipbuilding today [1]. In shipbuilding, the light weight composites and structural modules are more easily handled during construction. Thus, production time is decreased while also maintaining low production costs.

The U.S. Navy, in particular, has begun implementing composites into its superstructures and various other components above and below the waterline of its newer ships. The DDG-1000 *Zumwalt* class destroyer is the first U.S. Navy ship to use large-scale composite technology in its structural design. It will carry a superstructure and helicopter hanger composed of a resin transfer system scheme primarily with carbon fiber/vinyl ester skins and balsa wood and/or foam core. Implementation of these strong and lightweight materials above the waterline lowers the center of gravity which allows for the addition of more equipment while maintaining or even increasing the overall stability of the ship. As evidenced by many of the aluminum and steel craft employed by the U.S. Navy, corrosion is a major factor in the lifespan of a ship. Many studies are being conducted to combat the corrosion caused by seawater and large temperature gradients encountered in daily operations [2, 3]. Composites provide a reliable solution to this problem given that it does not corrode or decay and can remain in the water throughout its long life. However, there has been limited testing of composites in regard to its reliability and durability over many years of rigorous open ocean operations.

Once commissioned, ships in the U.S. Navy are typically expected to have an average lifespan covering 25 years of service [4]. Testing of composite materials must be conducted in order to provide continued performance as expected of these ships until which time they are decommissioned. These tests include, but are not limited to impact, fatigue, compression, and bend testing. As well, adhesion and damage tolerance must be conducted. The data gathered from these types of tests provide a range of information such as buckling loads, delaminating effects, bonding, and failure analysis which provide a breakdown of the projected performance characteristics and lifespan of composites.

B. OBJECTIVE

This study focuses on conducting a vibrational analysis of composite beams, similar to those used in marine applications, under conditions in which Fluid Structure Interaction (FSI) is occurring. Typically, ships on the open ocean will encounter many situations in which the structures are excited by various inputs. Excitation can occur from such inputs as the cyclical motion of waves, underwater explosions, or impact from debris and solid structures. The information gained will provide insight into the dynamic response of composites when subjected to these types of excitations. The added mass effect from FSI on composites in water is increased due to the relatively small differences in densities of the two. The composite beams were studied using clamped-free (cantilever) and free-free boundary conditions, both in air and fully submerged in water. The study contained herein utilizes two experimental techniques. First, the Digital Image Correlation (DIC) technique will measure the free vibration response of a cantilever beam subjected to an initial disturbance. Second, the more traditional approach of using an impact hammer and accelerometers will be utilized to determine the modes of vibration of a free-free beam. As well, the use of a high speed camera (HSC) system will provide real time images of the free vibration response of the composite beams. Collectively, the dynamic response of composites with FSI in water will provide crucial performance characteristics.

II. LITERATURE REVIEW

A. COMPOSITE MAKE-UP

Composites consist of multiple layers of reinforcing fibers bound together within a separate matrix material. The reinforcing fibers usually have high tensile and flexural strengths and moduli such as found in Kevlar, glass, and carbon composites while matrix materials include epoxies, aluminum, and titanium. The layers of fibers can be oriented in varying ways and combined with different matrix materials to produce optimal engineering properties for a specific design. This includes changing the bending stiffness, plane stiffness, and strength properties [5].

B. HISTORICAL PERSPECTIVE

Composite materials used in marine applications undergo numerous loading and unloading cycles throughout their lifespan. These cycles can produce damage within the composites that can virtually go undetected prior to failure which has placed an emphasis on testing composites under impact type events. Previous studies [6–9] have been conducted in order to give insight into the dynamic responses of the composites when subjected to these types of input forces including an array of FSI conditions surrounding marine composite structures. As well, other experimental and analytical studies [10–11] have been conducted to further the understanding of the free vibration response and modal characteristics of composite materials.

C. FSI OF COMPOSITES

Fluid structure interaction can be interpreted as an added mass effect as well as fluid damping to vibrating structures when in contact with a fluid medium such as water. The added mass effect changes the dynamic responses of the vibrating structure such as decreasing its natural frequency. This is especially significant regarding a composite structure since its density is close to the density of water. Studies [6–9] of composites under low velocity impact have also shown that there is an increase in impact force with samples tested while in contact with water due to the increase in total kinetic energy of

the fluid medium. The work of Owens [7] has shown that the natural frequencies of composite plates, when in contact with water on one side of the composite, decreases by approximately one-third of those tested in air. Kwak and Kim [10] calculated the non-dimensionalized added virtual mass incremental (NAVMI) factors for higher modes of clamped, simply supported, and free plates. These calculations were based on the assumption that the mode shapes remained the same while in contact with water. However, further tests by Kwak [11] determined that the modes shape for the fundamental mode of circular plates remained the same under the influence of water while changes in mode shapes were found at higher modes.

III. EXPERIMENTAL TECHNIQUES

A. DIGITAL IMAGE CORRELATION

1. Theoretical Background

The three dimensional (3-D) DIC technique is a noncontact, optical technique for obtaining full field deformation [12]. It utilizes a mathematical approach to analyze digital images taken of samples while undergoing mechanical testing. Changes in the surface characteristics of the specimen are captured by a stereoscopic system of two, charge-coupled device (CCD) cameras in consecutive images to record deformation and motion of speckle patterns on the specimen before and after deformation [12–16]. (Figure 1) Lighting is vitally important in acquiring clear and detailed images of the specimen being tested. In most cases, this can be accomplished through ambient lighting depending on the equipment set up and other factors such as f-number adjustments and aperture settings. Other standard white light sources or fiber optic lights may be used to supplement the ambient lighting. Once all the equipment has been set up and adjusted to achieve maximum performance, operation of the system can commence. The CCD cameras acquire an image of the surfaces of the specimen known as the reference image. Then a series of images are taken during and after deformation.

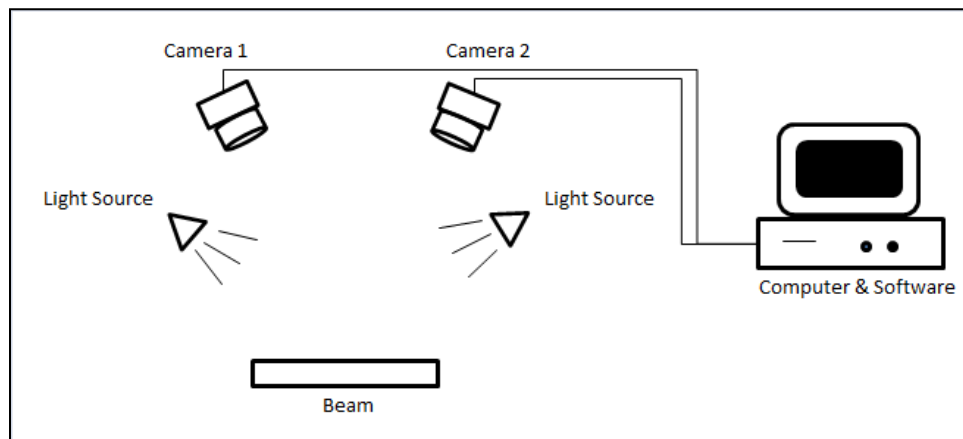


Figure 1. Typical stereoscopic setup

Each digital image contains light intensity measurements (gray scale values) for each pixel. These measurements are read as numbers ranging from 0 to 100 representing dark to light pixels, respectively [12]. Correlation is then used to locate the target from the given gray scale values of a defined subset of pixels surrounding a point of interest. Displacements u and v are thus determined by comparing two image subsets as shown in Figure 2.

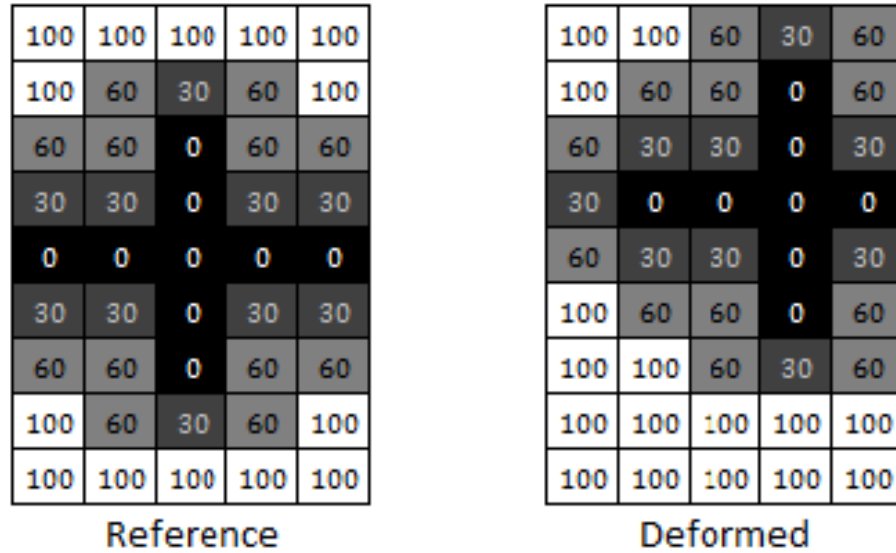


Figure 2. Subset of pixels before and after deformation. The speckle pattern has moved one pixel to the right and one pixel up. After [12]

2. Mathematical Background

Computer software is necessary to conduct DIC. This is accomplished by calculating the displacements u and v . For clarity, Figure 3 displays the reference and deformed configurations of a body on the same axis.

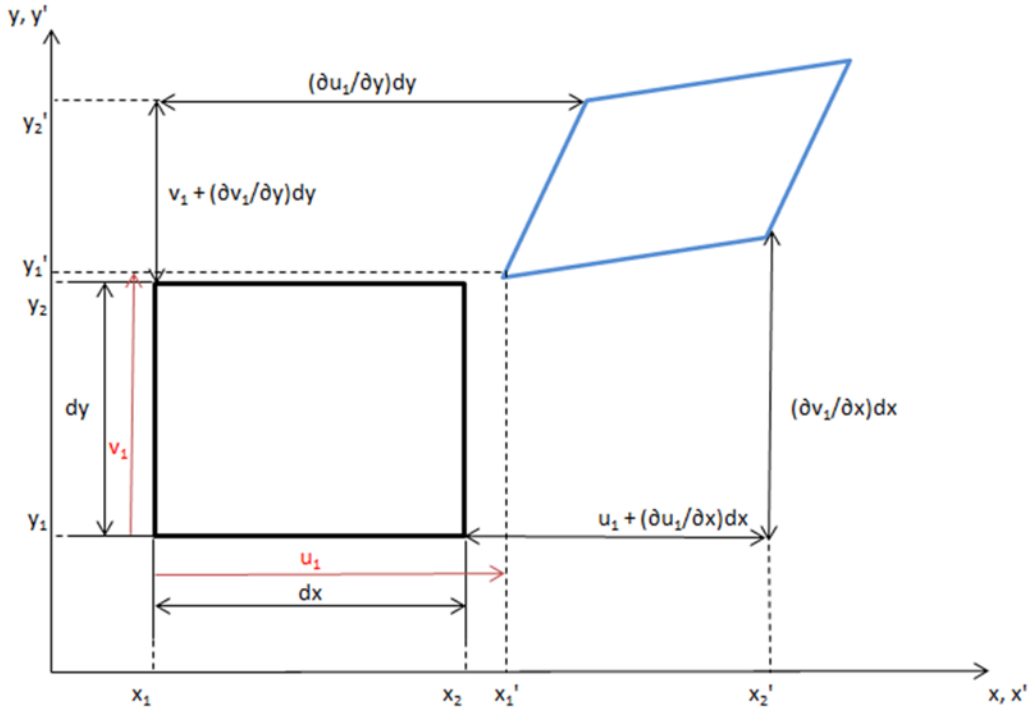


Figure 3. Graphical representation of the transformation between coordinates

Mapping the coordinates between two subsets is accomplished with the functions [13, 16]:

$$X = x + u(x, y) \quad (3.1)$$

$$Y = y + v(x, y) \quad (3.2)$$

With the use of a first order Taylor series expansion around the point (x_1, y_1) , the position of any point is given by:

$$x'_1 = x_1 + u_1 + \frac{\partial u_1}{\partial x} dx + \frac{\partial u_1}{\partial y} dy \quad (3.3)$$

$$y'_1 = y_1 + v_1 + \frac{\partial v_1}{\partial x} dx + \frac{\partial v_1}{\partial y} dy \quad (3.4)$$

where $dx = x_2 - x_1$ and $dy = y_2 - y_1$.

The correlation coefficient can be determined using several different approaches. One approach is to use a sum of squared differences. First, note that the correlation

coefficient is dependent upon a displacement vector $\bar{\mathbf{D}}$ which can be found by applying Equations (3.3) and (3.4). An iteration scheme must be applied to approximate the solution of $\bar{\mathbf{D}}$ in which the Newton-Raphson method can be used. Let $f(x_1, y_1)$ represent the undeformed gray scale value and $g(x'_1, y'_1)$ represent the deformed gray scale value. The correlation coefficient is then defined as:

$$C(\bar{\mathbf{D}}) = \frac{\sum_s [f(x_1, y_1) - g((x'_1, y'_1), \bar{\mathbf{D}})]^2}{\sum_s f(x_1, y_1)^2} \quad (3.5)$$

Since a digital image contains a multitude of pixels with discrete gray scale value gradients, it is necessary to apply a smoothing function. The process of interpolation smoothes the data over the entire field to optimize the gray scale values into continuous gradients at every location as shown in Figure 4. One of the most common types of interpolation used by DIC software is the bi-cubic interpolation function:

$$g(x', y') = \sum_{m,n=0}^3 a_{mn} \tilde{x}^m \tilde{y}^n \quad (3.6)$$

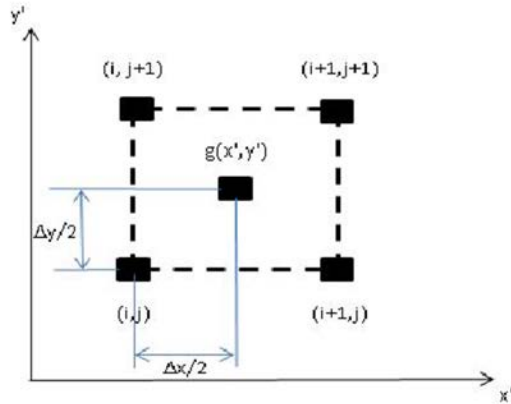


Figure 4. Optimization of pixel gray scale values

3. Specimen Preparation

In order for the specimen to be accurately studied, its surface must have a non-repetitive, isotropic, high contrast pattern often referred to as a speckle pattern [12]. This allows the software to determine the gray scale values and can be accomplished by

applying a multitude of black spots, with differing shapes, to a white background. Numerous methods exist that can achieve these results with relative ease. These include spray painting a white background followed by a fine black mist, blowing toner onto the specimen, or even adhering a computer generated speckle printout [12]. Information is obtained in greater detail using a finer pattern rather than a coarse one. The same is true for high-resolution (high pixel count) cameras.

Resolution is representative of the number of pixels in an image, the total number of pixels given in columns and rows. The space in which a pixel occupies can be determined by the proportionality of the resolution to the specimen dimensions. For example, if a 1216 x 912 resolution camera captures an image of a 200 mm x 50 mm specimen then the pixel space can be found by dividing the specimen width or height by the number of pixels in columns or rows, respectively [14,15]. For this case, the pixel occupies a space of 0.165 mm/pixel.

For accuracy, it is vital that the speckle pattern applied to the specimen is sized to fit the scale of the observation being made. An approximation of the customized speckle required for testing can be made by calculating the product of pixel space size and number of pixels desired for which the speckle covers [14]. (Figure 5) Continuing the above example, if it is desired for each speckle to cover five pixels the desired diameter of the speckle is approximated as 0.825 mm.

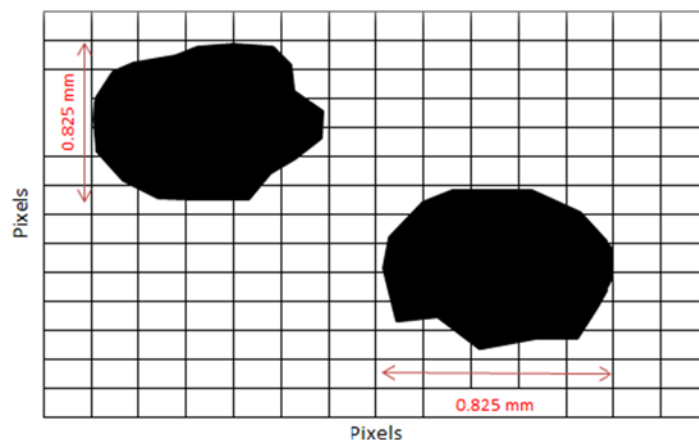


Figure 5. Example representation of speckle size per pixel

B. IMPACT HAMMER TEST

With ideal conditions being met, the impact hammer test is a method that would impact a structure with a Dirac impulse in order to excite all the modes of vibration [17]. One or more attached accelerometers are used to measure the response of the structure being tested. This measured response can either be static or dynamic acceleration in one, two, or three axes. Static acceleration is the measure of tilt angle with respect to the earth while dynamic acceleration is the measure of movement of the device [18]. The signals from test sensors are then processed through a charge amplifier to convert the signals to an analog voltage signal which can then be read into a dynamic signal analyzer (DSA). This, in turn, breaks the time signal down into individual frequencies. The typical setup for an impact hammer test is shown in Figure 6.

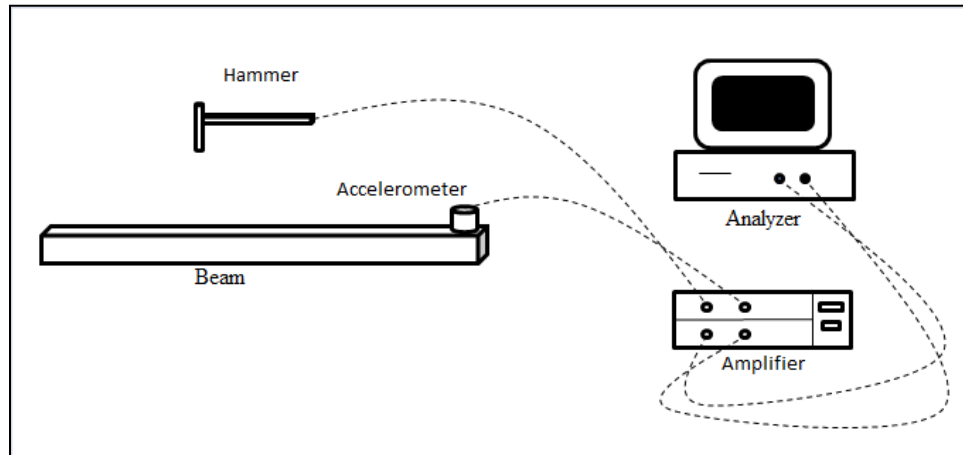


Figure 6. Typical impact hammer test setup

Impact hammers come in many sizes dependent on the experimental application. These range from the sledge-hammers used for testing large structures to lightweight hammers used for component testing. Various impacting tips are also used depending on the experimental application. Since an infinitesimally small (Dirac) impact cannot realistically be achieved, there is a known contact time of the hammer. As this contact increases, there is a decrease in the number of modes being excited. Thus, in order to excite a greater range of modes, a harder impact tip such as steel is required. Softer, plastic tips can be used to achieve smaller ranges.

C. MODAL ANALYSIS

1. Time Analysis

Modal analysis is conducted by measuring the vibration response of a structure over a specified time period. Deformation, velocity, and acceleration data can be acquired in the time domain by means of DIC or an impact hammer test as described above. Once the information is assembled and plotted as vibration vs. time, then the characteristics of the structure can be defined such as finding the maximum vibration level, period, and decay rate [19]. Here, the period T (sec) is the peak-to-peak time interval on the response plot. The period is inversely proportional to frequency f (Hz) as described by the equation:

$$f = \frac{1}{T} \quad (3.7)$$

If the natural circular frequency (rads/sec) is

$$w = 2\pi f \quad (3.8)$$

then

$$w = \frac{2\pi}{T} \quad (3.9)$$

As damping is introduced, oscillations begin to exponentially decay over time. If damping is increased to which the system does not oscillate, critical damping is achieved. The amount of damping is normally characterized by the ratio:

$$\zeta = \frac{c}{c_c} \quad (3.10)$$

where c is the amount of actual damping of the system and c_c is the critical damping coefficient. LDS-Dactron [19] expresses this relationship as:

$$\zeta = \frac{c}{2mw_n} \quad (3.11)$$

where m and w_n are the mass and undamped natural circular frequency, respectively. In the mass spring damper model, the mass and stiffness k are related to the natural frequency by:

$$w_n = \sqrt{\frac{k}{m}} \quad (3.12)$$

Thus,

$$\zeta = \frac{c}{2\sqrt{km}} \quad (3.13)$$

Given an initial magnitude X and time t , the decay rate of the system can be expressed as $Xe^{-\zeta w_n t}$. The damped natural frequency can then be expressed as:

$$f_d = f_n \sqrt{1 - \zeta^2} \quad (3.14)$$

2. Frequency Analysis

Further information about the vibration of a structure can be gained by transforming the time domain signal into the frequency domain. It has many advantages such as being able to cover a broad range of frequencies for analysis [20]. This is accomplished through a mathematical method known as the Fast Fourier Transform (FFT). The FFT is an improved Discrete Fourier Transform algorithm that makes use of repeating terms in the range of frequencies and reduces the number of operations, given by the equation [20]:

$$X(f_n) = \int_{-\infty}^{\infty} x(t) e^{2\pi i f_n t} dt \quad (3.15)$$

where $x(t)$ and $X(f_n)$ are the time signal and its Fourier transform, respectively. In order to sufficiently represent the signal, the Nyquist critical frequency

$$f_c = \frac{1}{2\Delta t} \quad (3.16)$$

must be satisfied in which the sampling period Δt should be at least half of the period of the signal [20].

IV. TEST EQUIPMENT

A. WATER TANK AND TESTING APPARATUS

The water tank is constructed of 0.5 in (12.7 mm) thick plexiglass with inner dimensions of 23 x 11 x 18 in (584.2 x 279.4 x 457.2 mm). (Figure 7) Each piece is bonded together with Weld-On 40 acrylic glue. It has a bond strength of 4000 psi following a one week cure time at room temperature [21]. The tank was placed on a sturdy laboratory table where the tests were to be conducted. Tape was then used to mark the exact location of the tank of the table to ensure its position in each test. Additionally, a grease pencil outlined the exact area in which the mobile cantilever testing apparatus was to be placed in the tank. It was filled with 19 gallons of distilled water and covered when not in use to limit the amount of dust and other particles that could potentially interfere with the accuracy of the DIC test.



Figure 7. Image of water tank

The cantilever testing apparatus was constructed of steel. First, a 10 x 2.5 x 1.25 in (254 x 63.5 x 31.75 mm) piece of steel was used as a base with two other 1.25 x 1.25 in (31.75 x 31.75 mm) square pieces of steel mounted to the base to provide a stable platform and clamping mechanism for the composite beam. The clamping mechanism allows for 0.75 in (19.05 mm) of the composite beam to be held in place with two Allen screws passing through each. An 8 x 1.25 x 1.25 in (203.2 x 31.75 x 31.75 mm) aluminum I-beam was placed behind the clamping mechanism and attached to the base. This provides a guide for the fishing line attached to each beam as described in section D of this chapter. It also provides a maximum for the initial displacement of the beam. Figure 8 is an image of the cantilever device. Constructing it in this way allows the cantilever testing apparatus to be mobile enough to remove from the water tank in order to replace the composite beams while maintaining a viable support for testing.



Figure 8. Image of cantilever testing apparatus

B. DIC SETUP

Careful attention was made when setting up and adjusting the stereoscopic CCD cameras. The CCDs are attached to a vertical mounting beam attached to a tripod. This allows for adjustments relative to the mechanism in which the composite is being tested, ensuring the proper focal length to acquire clear images. The mounting beam also allows for the CCDs to be spaced symmetrically about the specimen in order to achieve the proper stereo angle. The stereo angle is based on the type of lens being used. Here, 35mm lenses are being used which require a stereo angle of at least 20° , with 60° being the absolute limit. All calculations for spacing requirements in this setup use a stereo angle of 25° . Simple geometry can be used to determine these requirements; however, testing the composite beams in water brings forth a couple of challenges that cannot be overlooked. Figure 9 shows the initial spacing required for gathering accurate results with the composite beam in air.

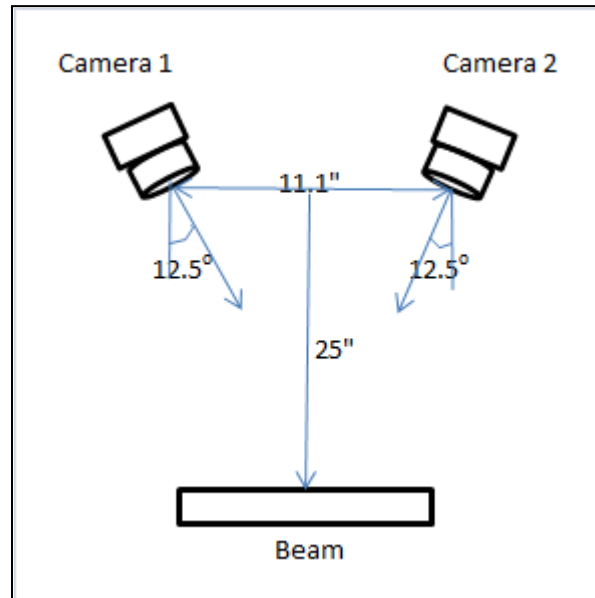


Figure 9. Initial DIC set up with spacing dimensions

1. Special Considerations for Testing in Water

a. Magnification of Composite Beam

Due to refraction, the water medium enlarges the image captured in DIC testing. According to Ross et al. [22], the degree to which the composite beam is magnified can be calculated using the equation:

$$M = m \left\{ \frac{[1 + (d + R) / D]}{[1 + m(d + R) / D]} \right\} \quad (4.1)$$

where $R = 0.8$ and $m = 1.33$.

R is the radius of curvature for the camera lens, m is the index of refraction for water, D is the distance (in cm) from the beam to the plexiglass, and d is the distance (cm) from the camera to the plexiglass. M is thus, the image magnification. Adjustments were made in order to capture the length of the beam. The final distance between the composite beam and the camera was determined to be 30.25 in (76.84 cm). Since the distance D is equal to 11.75 in (29.85 cm) the cameras were set to a distance d equal to 18.5 in (46.99 cm) from the tank. This yields an image magnification of 1.138. Therefore, the composite beam appears to be approximately 13.8% larger in water than in air for each CCD. This equates to an apparent beam length of 9.10 in (23.11 cm). This is valid assuming the initial displacement of the beam is small.

b. Light Refraction and Reflection

To eliminate the reflection of light from the free surface of the water, the CCD cameras were aligned vertically from one another on the mounting beam in order to capture images from the side of the water tank. As well, the lighting system was consisting of two *Lowell Pro* lights were placed at angles from below the waterline to achieve a uniform spread across the composite beam. This essentially eliminated all of the reflected light to the CCD's. Light refraction through the plexiglass and water also affects the stereo angle of the system. Achieving the desired stereo angle is accomplished through the use of Snell's Law which, in mathematical form states:

$$n_1 \sin(\theta_1) = n_2 \sin(\theta_2) \quad (4.2)$$

where the subscripts one and two represent the initial medium from which the light originates and the secondary medium through which light refracts.

Solving for either θ_1 or θ_2 for light passing from a water medium into plexiglass and then from the plexiglass to air allows for the determination of the initial and final stereo angles. To achieve the desired minimum 25° stereo angle, the relative stereo angle of the CCD's must be 33.4° . The operational set up, with all adjustments being complete, is shown in Figure 10.

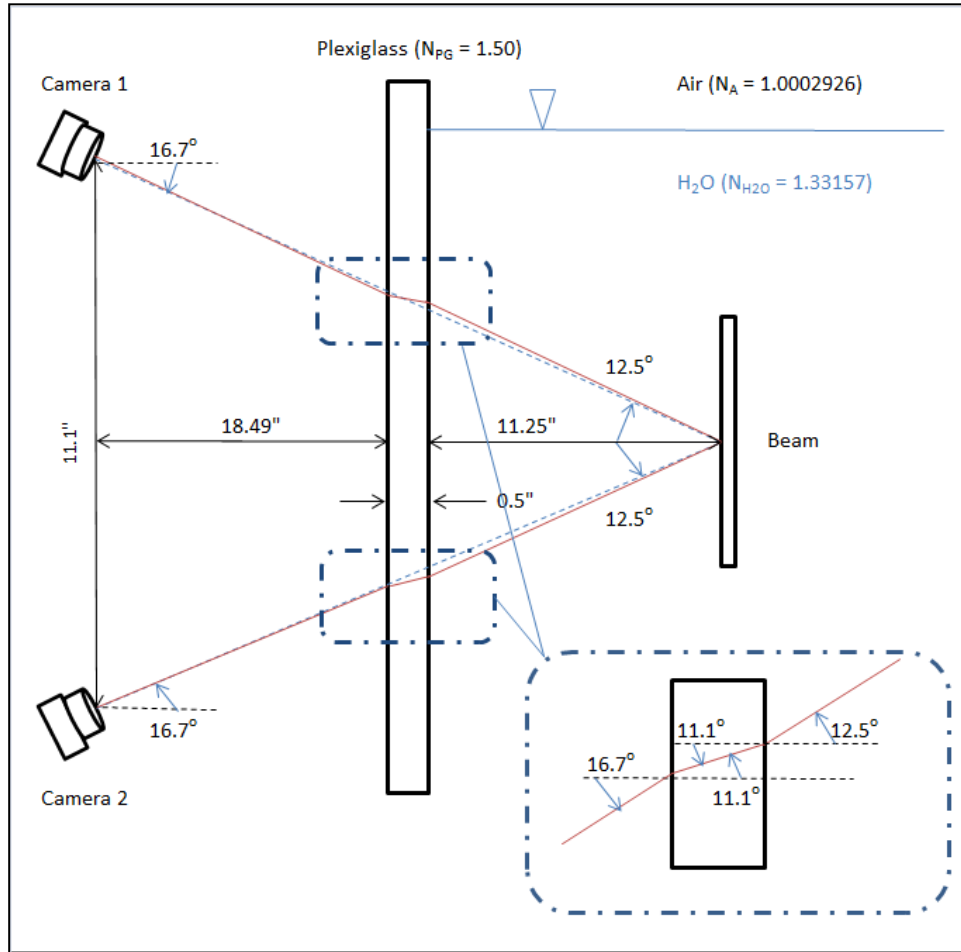


Figure 10. Operational DIC set up

C. IMPACT HAMMER SETUP

Since this test was conducted in air and while submerged in water, the accelerometers needed to be waterproofed prior to any tests being conducted. Waterproofing was accomplished by applying two light coats of barrier A to the accelerometers (with cables attached) allowing three days to set between coats. This was followed by another two light coats of RTV with two days of set time between each coat. Since the impact hammer could not be reasonably waterproofed, a 9 x 1 x 0.325 in (228.6 x 25.4 x 8.26 mm) lightweight balsa-cored sandwich composite beam was vertically attached to the end of the test beam with super glue. This allowed the balsa-core sandwich composite to extend 0.5 in (12.7 mm) out of the water and provided a dry striking platform for the impact hammer. A second balsa-core sandwich composite beam was also vertically attached to the opposite end of the test beam in order to evenly distribute the mass across the length of the beam. It also gave the same conditions for fluid flow around each end of the beam. Since the goal of this experiment was for the comparison of the vibration response of the beam in air and in water, it is reasonable to utilize this setup. By doing this prior to any testing, it provided the same conditions for the total mass in each test.

Following the fabrication of the composite beams and waterproofing of the test equipment, 10 accelerometers were evenly spaced and glued to the underside of the test beam. The exact location and spacing of the accelerometers are illustrated in the SolidWorks drawing in Appendix A. The impact hammer and accelerometers were then routed to through an amplifier for conversion into an analog signal and then routed to the DSA for data acquisition and analysis much like the setup as shown in Figure 6.

The water tank for this experiment was placed on a mobile cart to facilitate testing for each test environment. The test beams were leveled at a distance of 36.75 in (933.45 mm) above the ground. This ultimately placed the test beams in the center of the water level in the tank. Figure 11 shows the setup for the impact hammer test.

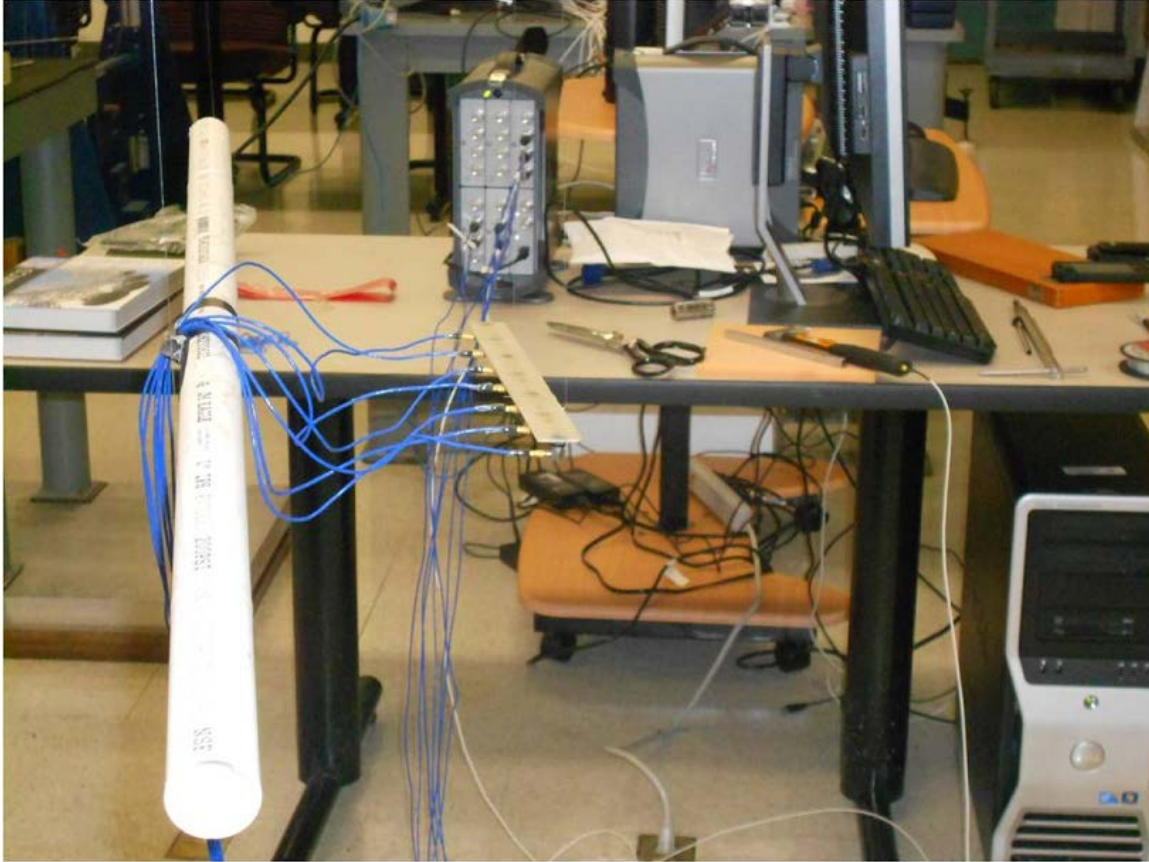


Figure 11. Image of impact hammer test setup

D. COMPOSITE SELECTION

1. Overview

The composite beam test samples were constructed using the Vacuum Assisted Resin Transfer Molding (VARTM) technique to mimic the technique used in marine construction. Each composite sample consists of varying layers of non-biased, plain weave 6 ounce E-glass laid at both $0^{\circ}/90^{\circ}$ and $\pm 45^{\circ}$ orientations. The vinyl ester resin used for this process was Derakane 510A-40 epoxy and was cured at room temperature for 24 hours followed by two hours at 120°C (250°F). Strength data for the epoxy vinyl ester resin is provided in Table 1. Table 2 provides an overview of the composite sample dimensions being used in this study.

Table 1. Associated Strength Properties of Derakane 510A-40 Epoxy Vinyl Ester Resin After [23]

Property of Clear Casting at 25°C (77°F)	Value (MPa)	Value (kpsi)
Tensile Strength	86	12.3
Tensile Modulus	3400	490
Flexural Strength	150	21.7
Flexural Modulus	3600	520

Table 2. Overview of composite sample dimensions and orientation

DIC Test Composite Samples							
# Layers	Orientation	Length		Width		Thickness	
		in	mm	in	mm	in	mm
6	0°/90°	8.75	222.25	1	25.4	0.048	1.219
6	+/-45°						
Impact Hammer Test Composite Samples							
# Layers	Orientation	Length		Width		Thickness	
		in	mm	in	mm	in	mm
16	0°/90°	11	279.4	1	25.4	0.105	2.667
16	+/-45°						

2. DIC Test Composite Samples

For DIC testing and HSC images, the composites consisted of six layers of non-biased, plain weave 6 oz E-glass. Ten samples of each ply orientation were made with unclamped dimensions of 8 x 1 x 0.048 in (203.2 x 25.4 x 1.22 mm). These dimensions were chosen to allow the specimen to cover the field of view along the horizontal axis. As well, when subjected to an initial disturbance the corresponding free vibration is low enough to be captured by the low-speed cameras. To ensure accurate deformation/displacement measurements, it is vital to apply a good speckle pattern. For this experiment, the speckle pattern was applied using the spray paint technique. First, a base coat of flat white paint was sprayed on the surface of the composite. Once dried, a thin black mist was applied to create the speckle pattern. This was accomplished by inverting the spray can and throttling the nozzle approximately two feet above the specimen. In doing so, a properly sized and spaced speckle pattern was customized for

this experiment. All sides of the composite samples where cuts were made were also painted to prevent water intrusion into the core. As testing progressed, it was desired to gain further detail along the composite beam. Thus, a finer speckle pattern needed to be achieved. Figure 12 and Figure 13 show the customized speckle patterns as described above.



Figure 12. Customized speckle patterns. (a) Coarse speckle pattern. (b) Fine speckle pattern

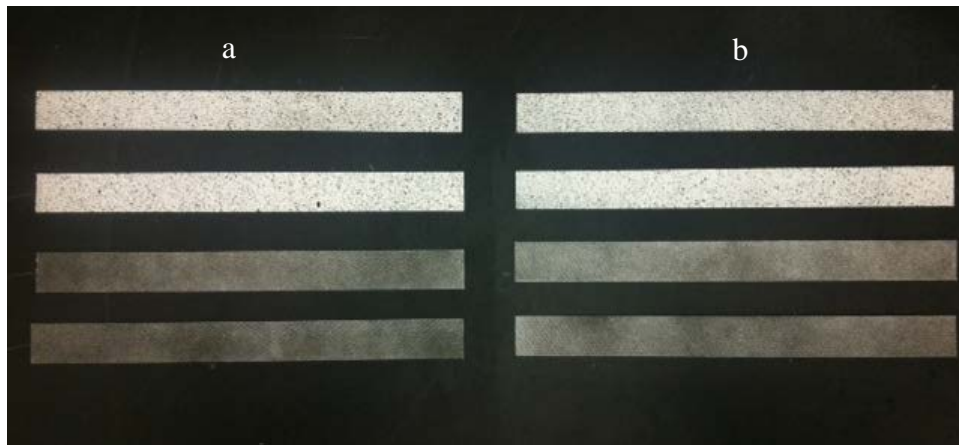


Figure 13. Image of fabricated composite samples for DIC tests. (a) $0^{\circ}/90^{\circ}$ orientation. (b) $\pm 45^{\circ}$ orientation

An 18 in (457.2 mm) piece of 6 lb test fishing line was bonded to the tip of each composite sample. This was accomplished by placing one drop of superglue on the line in the center of the width of the sample. This allows for the beam to be initially displaced a specified distance and then released to vibrate freely. Herein this study, the mass of the fishing line and superglue are assumed to be negligible.

3. Impact Hammer Test Composite Samples

For the impact hammer test, the composites consisted of 16 layers of non-biased, plain weave 6 ounce E-glass. One samples of each ply orientation were made with the dimensions of 11 x 1 x 0.105 in (279.4 x 25.4 x 2.67 mm). These dimensions were chosen to allow water domain to be at least four times the area of the beam as it is held in a free-free condition in the center of the water tank [11]. In addition, 16 layers were used to increase the stiffness of the beams in order to provide a good base to which the accelerometers could be attached.

V. TEST CONDITIONS

A. OVERVIEW

For DIC testing, the composite samples and CCD cameras were placed vertically to capture images through the sides of the water tank due to the reflection from the free surface of the water. As for the impact hammer testing, two lengths of 6lb test fishing line were suspended from the ceiling with a rubber band link between each to hold the beam in a free-free condition.

B. TEST SAMPLE ENVIRONMENTS

1. In Air

Initial testing was conducted in air to provide a baseline for comparison with all other conditions of testing. It is used to identify the differences in responses of the composite samples with FSI in water. For DIC testing, the beams were held in the cantilever testing apparatus. For the impact hammer testing the beam was held in a free-free condition with 6lb test fishing line suspended from the ceiling with a rubber band link between each and loosely tied around the beam at its predicted first mode nodal points. Additionally, testing of the composites was conducted a second time after the tests while submerged in water to ensure water intrusion did not affect the samples.

2. Submerged in Water

The water tank was filled with approximately 18.6 gallons of distilled water bringing the water level to 17 in (431.8 mm) above the bottom of the tank. For DIC testing the water level was 5.25 in (133.35 mm) above the tip of the composite beam after being placed in the support. The water level for the impact hammer testing was 8.5 in (215.9 mm) above the sample as it was suspended in the center of the water tank in its free-free condition. Using distilled water limited the amount of particles in the water that could adversely affect the images during DIC testing.

C. TEST PROCEDURES

1. Preliminary Calculations

a. *Material Properties of Composite Samples*

A standard three-point bend test was conducted to approximate the bending stiffness EI in order to calculate the theoretical frequencies of the composite beams with the given boundary conditions. This test was conducted using five samples of each layer sequence. An *Instron* testing system was utilized to measure and record force and deflection data. The bending stiffness was averaged over the five samples of each sequence using Euler-Bernoulli beam theory, where the deflection of a simply supported beam with a span length L and a center-wise applied force P gives the maximum deflection δ as:

$$\delta = \frac{PL^3}{48EI} \quad (5.1)$$

Solving for the bending stiffness yields:

$$EI = \frac{PL^3}{48\delta} \quad (5.2)$$

In addition, the density ρ was approximated by measuring the mass m to the nearest 0.01 gram and volume V to the nearest 0.001 in³ of each beam where:

$$\rho = \frac{m}{V} \quad (5.3)$$

Table 3 and Table 4 provide the bending stiffness and density of each beam as determined by the methods described, respectively.

Table 3. Measured bending stiffness of each beam sequence

Sample		EI (Nm ²)
6-Layer	0°/90°	0.073766
	±45°	0.05936
16-Layer	0°/90°	0.266573
	±45°	0.15292

Table 4. Measured density of each beam sequence

Mass		Length		Width		Thickness		Volume	Density
g	kg	in	m	in	m	in	m	m ³	kg/m ³
6-Layer									
15.56	0.01556	11.224	0.2851	1.011	0.0257	0.047	0.00118	8.65E-06	1799
16-Layer									
23.87	0.02387	11.001	0.2794	1.025	0.0260	0.073	0.00183	1.33E-05	1793

b. Theoretical Natural Frequency of the Cantilever Beam

In order to determine the camera settings for the DIC testing technique, the frequency of vibration must first be determined. Several methods exist for determining the theoretical natural frequency of a vibrating cantilever beam. However, for purposes of this study only two methods will be explored in order to bracket the natural frequency expected as it will be used for further calculations in running the DIC test. The first method in determining the natural frequency of a cantilever beam is to model the system as a discrete system. With the mass being evenly distributed along the length of the beam, this method assumes the beam to be mass-less with the entire mass of the beam concentrated at the tip of the free end. Taking one third of the mass at the tip yields the mass equation:

$$m_{total} = \frac{33}{140} m_{beam} \quad (5.4)$$

Plugging this mass into Equation 3.12 with Equation 3.8 where

$$k = \frac{Force}{Deflection} = \frac{3EI}{L^3} \quad (5.5)$$

yields:

$$f_n = \frac{1}{2\pi} \sqrt{\frac{3EI}{m_{total} L^3}} \quad (5.6)$$

Here the bending stiffness, mass and length can be measured in order to determine the natural frequency. Using the data contained in Table 4 for the six-layer, 0°/90° orientation composite sample, the fundamental frequency is 13.49 Hz. The system can

also be modeled as a continuous system in which its natural frequency is given in terms of a constant $\beta_n L$ corresponding to the normal modes of oscillation. If,

$$\beta = \left(\frac{12\rho w^2}{Et^2} \right)^{1/4} \quad (5.7)$$

then

$$f_n = \frac{1}{2\pi} \sqrt{\frac{\beta_n^4 Et^2}{12\rho L^4}}; \quad n = 1, 2, 3, \dots \quad (5.8)$$

The values $\beta_n L$ for the first three modes are listed in Table 5.

Table 5. Values for $\beta_n L$ for the first three modes of a cantilever beam

Mode	$\beta_n L$
1	1.875
2	4.694
3	7.855

Research in determining the value of the modulus of elasticity ranges from 15.7GPa to 21GPa. Therefore, an approximation can be made using the equation:

$$E = \left(\frac{M}{L} \right) \left(\frac{12}{bt^3} \right) (2\pi f_n)^2 \left(\frac{l^2}{[\beta_n L]^2} \right)^2 \quad (5.9)$$

where

- M is the total mass of the beam.
- L is the total length of the beam.
- b is the width of the beam.
- t is the thickness of the beam.
- f_n is the Mode 1 natural frequency as determined in Equation 5.6.
- l is the free length of the beam.
- $\beta_n L$ is the value corresponding to the Mode 1 natural frequency in Table 5.

Using the same values as in Equation 5.6, the modulus of elasticity was determined to be 15.9 GPa for the composite beams used in this study. Placing this value into Equation 5.8, the fundamental frequency is 13.37 Hz. Since vibration of the cantilever beam is

higher in air than water, this value of the average fundamental frequency of 13.43 Hz will be used for follow-on calculations for DIC testing procedures.

c. Theoretical Natural Frequency of the Free-Free Beam

As a continuous system the free-free beam was modeled in much the same way as the cantilever beam with the exception of the boundary conditions. Here, the values for $\beta_n L$ are as listed in Table 6. Note that where $n = 0$, there is a rigid body mode.

Table 6. Values for $\beta_n L$ for the first four modes of a free-free beam

Mode	$\beta_n L$
0	0
1	4.73
2	7.853
3	10.995

The natural frequency is then given by:

$$f_n = \frac{1}{2\pi} \frac{(\beta_n L)^2}{L^2} \sqrt{\frac{EI}{\rho A}} \quad (5.10)$$

in which $A = bt$. The fundamental frequency of the 16-layer, $0^\circ/90^\circ$ orientation composite beam is 71.57 Hz.

Due to the addition of mass by the 10 accelerometers, it is reasonable to expect that the experimental natural frequency will be lower than the theoretical natural frequency. Accounting for the mass of the 10 accelerometers, Equation 5.10 becomes:

$$f_n = \frac{1}{2\pi} \frac{(\beta_n L)^2}{L^2} \sqrt{\frac{Ebt^3 L}{12(m_{beam} + m_{accels})}} \quad (5.11)$$

The fundamental frequency then becomes 52.9 Hz. This value will be used to determine the sampling rate needed for the impact hammer test.

2. DIC Test Procedure

Since the DIC technique is accurate to approximately 0.02 pixels, the exposure time should be set to contain the motion of the object to this value or less [24]. The field

of view for the 1628 x 1236 cameras is 8.5 x 6.25 in (215.9 x 158.8 mm). Here, the magnification is about 0.13 mm/pixel. Thus, the ideal motion needs to be below 0.0026 mm. The equation of motion for the cantilever is given as:

$$X_m = X_0 \sin(w_n t + \phi) \quad (5.12)$$

where X_m is the amplitude of the resulting motion and w_n is the natural frequency of the beam in rads/sec. Thus, taking the derivative of Equation 5.10 yields:

$$\dot{X}_m = X_0 w_n \cos(w_n t + \phi) \quad (5.13)$$

which gives the maximum velocity of the cantilever as 107.5 mm/s. The ratio of the maximum motion to maximum velocity results in a maximum exposure time of 24 μ s. However, given there is little pixel movement with the out of plane motion of the beam and the use of halogen lighting, it is reasonable to set the exposure time to 100 μ s in order to achieve accurate results without any blur in the images. Testing the beam while submerged in water greatly reduces the velocity given that the frequency of vibration is reduced by approximately one third [7]. Therefore, the same exposure time can be set for tests in air and in water.

Given the period of vibration of the cantilever beam as 72.89 ms, the sampling rate for the DIC test should be set to a minimum of 36.44 ms to satisfy the Nyquist critical frequency [20] as found in Equation 3.16. However, the use of the low speed cameras in this test will not allow for this sampling rate. Thus, the sampling rate was set to capture images at a rate of 5 Hz. In other words, images are captured every two and a half periods. This is sufficient only in visualizing the displacements of the beam at specific times as a linear combination of mode shapes. In water, the period decreases to approximately 220 ms which will provide the same visualization of displacements at specific instances of time. Due to the inability of the CCDs to reach the desired sample rate, a separate HSC was utilized in conjunction with the DIC testing in order to estimate the frequency of vibration of the composite beams. The HSC was placed perpendicular to the edge of the beam and the sampling rate was set to 1000 Hz. The exposure time was set to 20 μ s.

Once the exposure time and sampling rate were set, a 12 x 9 grid with 9 mm spacing was used to calibrate the stereoscopic camera system for testing. Following calibration, an index picture was taken to provide a basis for correlation. Then the beam was displaced with the attached fishing line and released at the same instance the cameras were triggered. The cameras recorded images for fifteen seconds at the set sampling rate which yielded 77 images for each of the tests. Ten separate composite beams were tested of each ply orientation in air, then while submerged in water, followed by a second round in air. The acquired data was post-processed using the *VIC-3D* software in which the correlation was run with a subset of 21 pixels at a step of 5 pixels. A smoothing function was applied to the Z-coordinated and displacement data utilizing a decay filter of 15 pixels. All errors and calibration parameters were recorded for each correlation.

3. Impact Hammer Test Procedure

The period corresponding to the highest natural frequency of interest (16-layer, 0°/90°, Mode 3) is 2.59 ms. Thus the sampling rate of the DSA was set to 500 Hz which corresponds to 2 ms and meets the Nyquist criterion [20]. Due to the inability to waterproof the impact hammer for testing in composite beams submerged in water, a six inch steel rod was held on the beam and tapped with the hammer to transfer the force to the beam. The rod was removed immediately after impact and prior to the rebound of the beam. Any test where the rebound resulted in contact with the rod was discarded and repeated.

The accuracy of this method was tested on an aluminum beam with dimensions of 11 x 1 x 0.25 in (279.4 x 25.4 x 6.35 mm). It was outfitted with 10 accelerometers evenly spaced along the centerline of the beam in the same way as the composite beams. First, the beam was struck with the impact hammer only at the center of the end directly over the first accelerometer. This test consisted of five frames for averaging. Figures 14–16 detail the natural frequencies and corresponding mode shapes of the first three modes from this test. A second test was conducted by striking the steel rod as it was held in the same location as the previous test. Again, five frames were represented for averaging. Figures 17–19 detail the natural frequencies and corresponding mode shapes of the first

three modes. Table 7 shows the theoretical and natural frequency of all three modes for each impact method. It appears that impacting a steel rod resting on the composite beam and removing it prior to rebound has little, if any, effect on the accurate vibration testing. Mode shapes are identical in both methods with less than a third of a percent difference in natural frequencies. With the validation of this method, it was utilized for all testing whether in air or in water to provide consistency among testing.

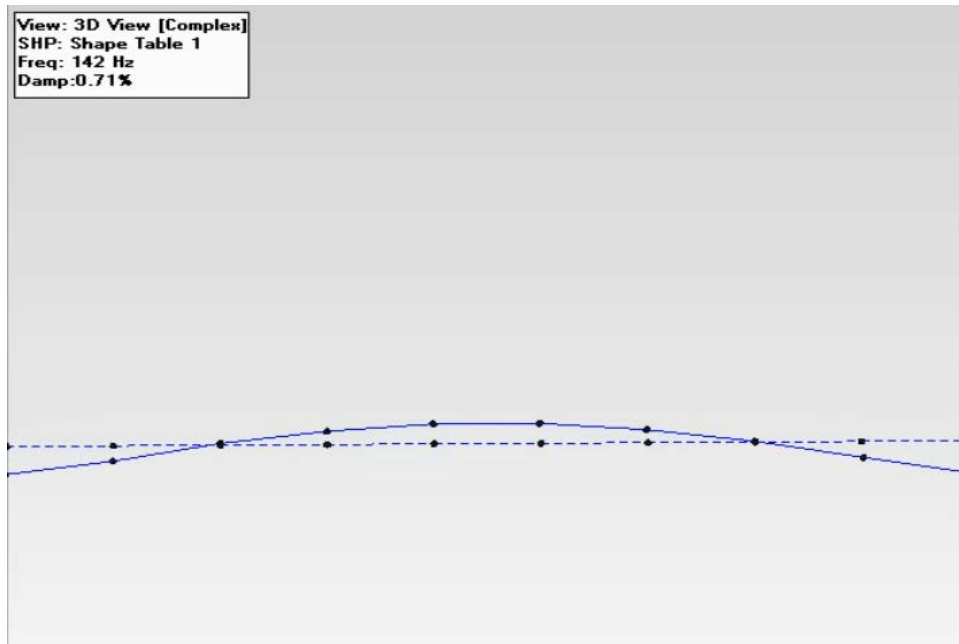


Figure 14. Mode 1 of free-free aluminum beam struck by impact hammer only

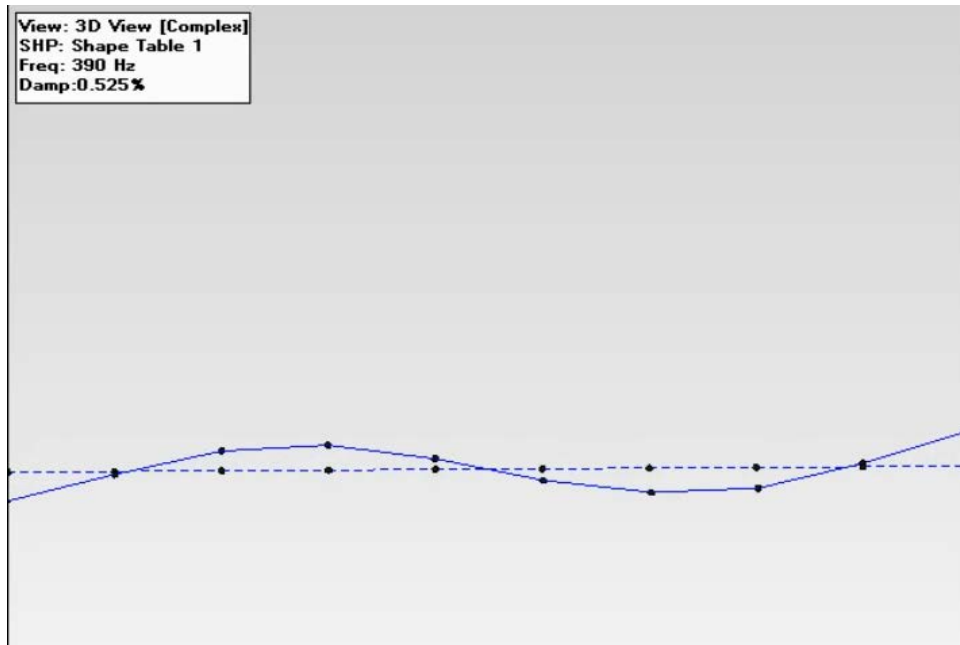


Figure 15. Mode 2 of free-free aluminum beam struck by impact hammer only

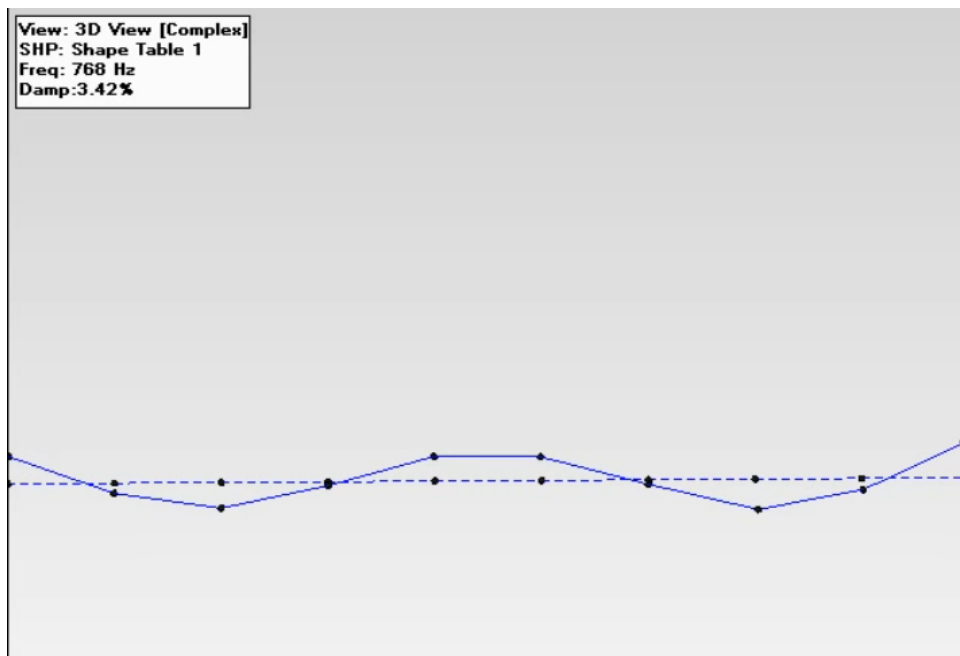


Figure 16. Mode 3 of free-free aluminum beam struck by impact hammer only

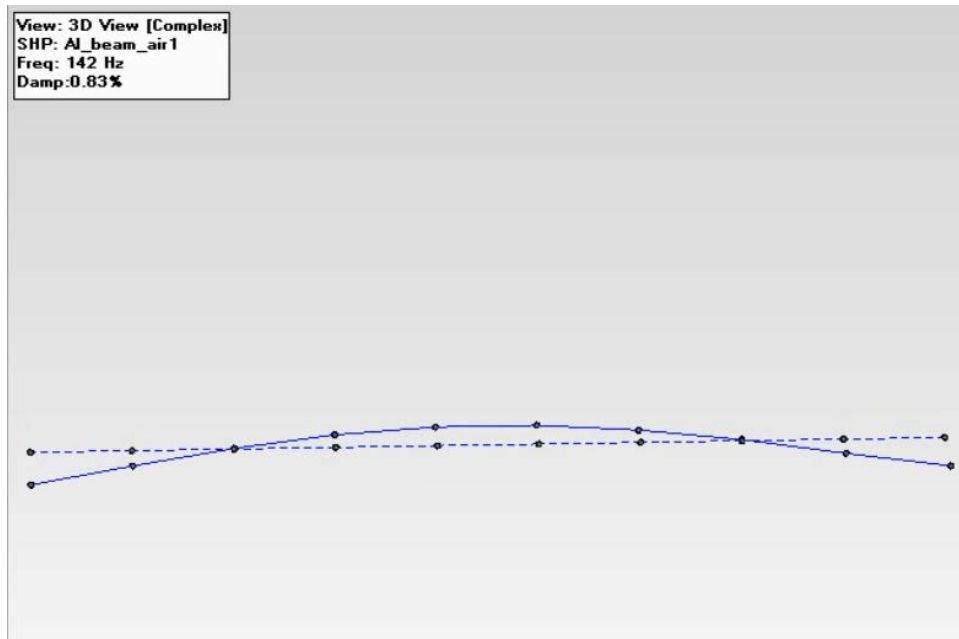


Figure 17. Mode 1 of free-free aluminum beam struck by impact hammer with the steel rod

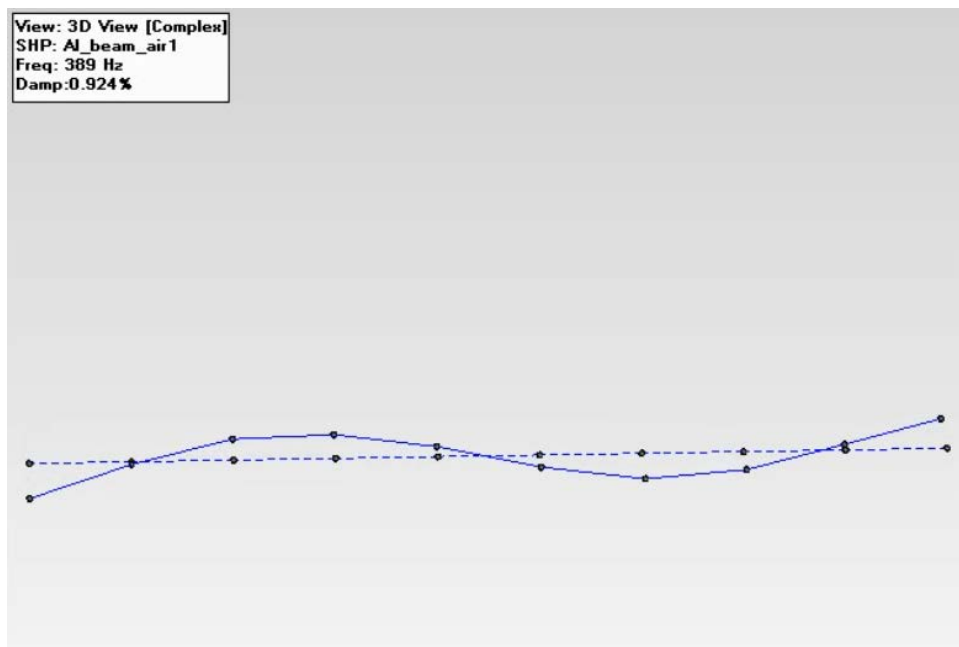


Figure 18. Mode 2 of free-free aluminum beam struck by impact hammer with the steel rod

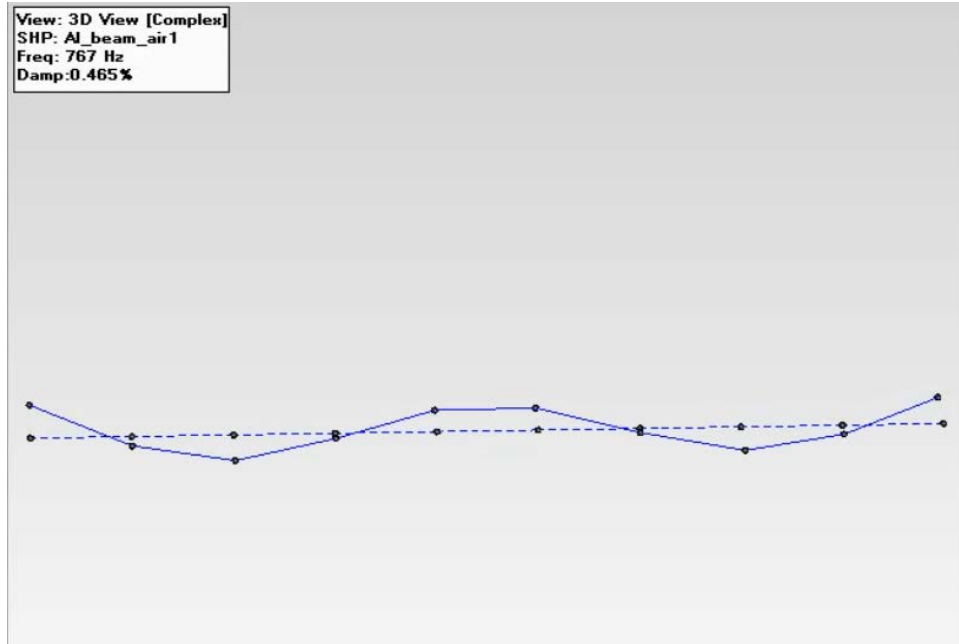


Figure 19. Mode 3 of free-free aluminum beam struck by impact hammer with the steel rod

Table 7. Natural frequencies for Modes I, II, and III for each method for free-free beam aluminum beam in air

	Mode	Natural Frequency (Hz)				
		Theoretical	f_d	ζ	f_n	% error
Impact Hammer Only	1	144.66	142	0.0071	144.66	0.003
	2	398.75	390	0.00525	398.76	0.001
	3	781.65	768	0.0342	782.11	0.059
Impact Hammer & Steel Rod	1	144.66	142	0.0083	144.66	0.001
	2	398.75	389	0.00924	398.77	0.003
	3	781.65	767	0.00465	781.66	0.057

Data for each composite beam test was acquired in 25 frames to produce an average. One 16-layer composite beam of each orientation was tested in air and submerged in water. Following acquisition, the data was post-processed for analysis using the *VSME Scope* software.

THIS PAGE INTENTIONALLY LEFT BLANK

VI. RESULTS AND ANALYSIS

Initial testing in air was completed to provide a baseline for comparison with all other testing environments. Testing was then conducted in a water environment in order to determine changes in the free vibration response. This was followed by more testing in air to show repeatability and to show that water intrusion is not a factor needing to be considered. Samples of each orientation with the fine speckle pattern were not used for analysis due to aliasing of the data. Figure 20 shows the presence of the moiré pattern on a representative sample. This is likely due to the high resolution of the pixels in the image.

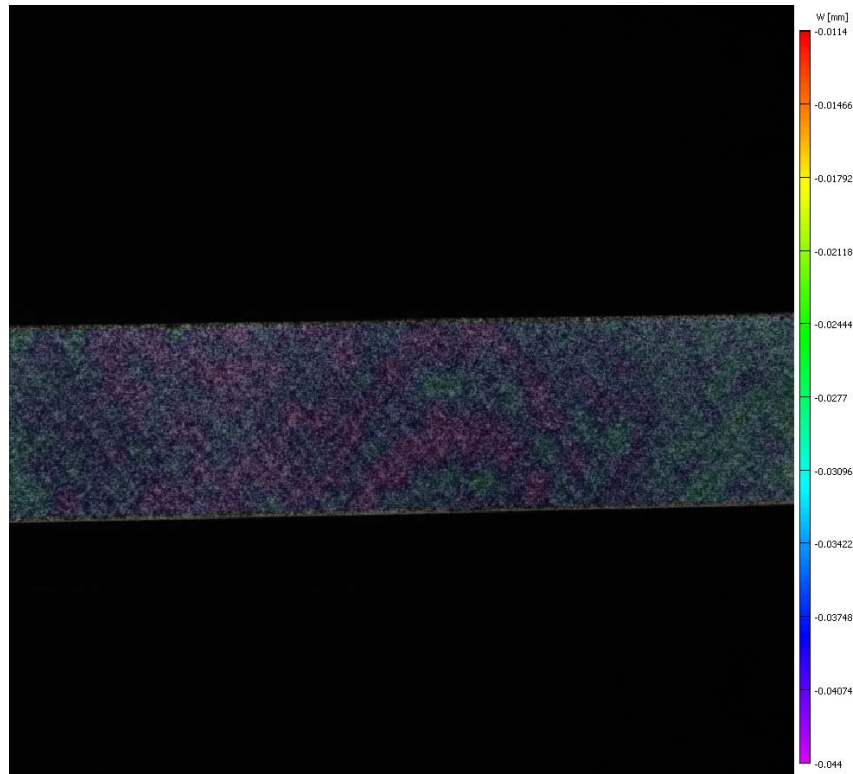


Figure 20. Typical moiré pattern on representative sample with fine speckle pattern

A. DIC TEST

1. Validation between Test Environments

Figure 21 illustrates a representative sample of the displacement of the composite beam in the water environment as compared to its baseline in air. This is used as a

measure of validation in that acquiring images with the CCDs through a water medium is accurate when compared to images acquired through an air medium. The tip of the beam was displaced 0.75 in (19.05 mm) which was measured along the length of the beam in both air and water environments. This measure consisted of 100 evenly spaced points along the centerline of the beam as shown in Figure 22. As shown in Figure 21, there is good agreement between the displacements in each of the testing environments. However, there is a slight discrepancy at the tip of the beam. There is a about a 2% difference in the tip displacements from each environment. This difference may be due to the distortion of the image at the tip caused by amplitude in the out-of-plane displacement.

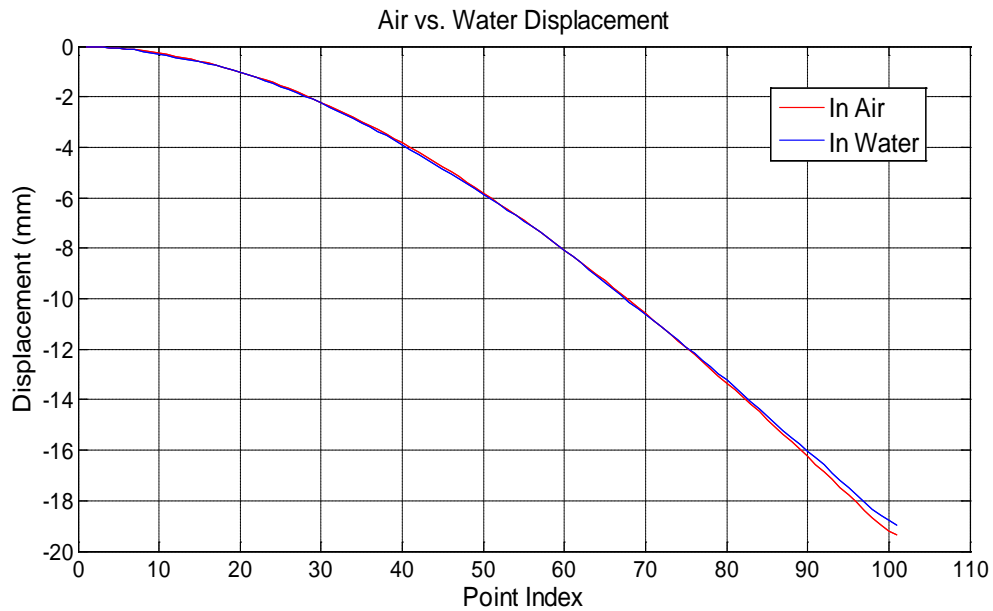


Figure 21. Displacement of composite beam in air and water environments

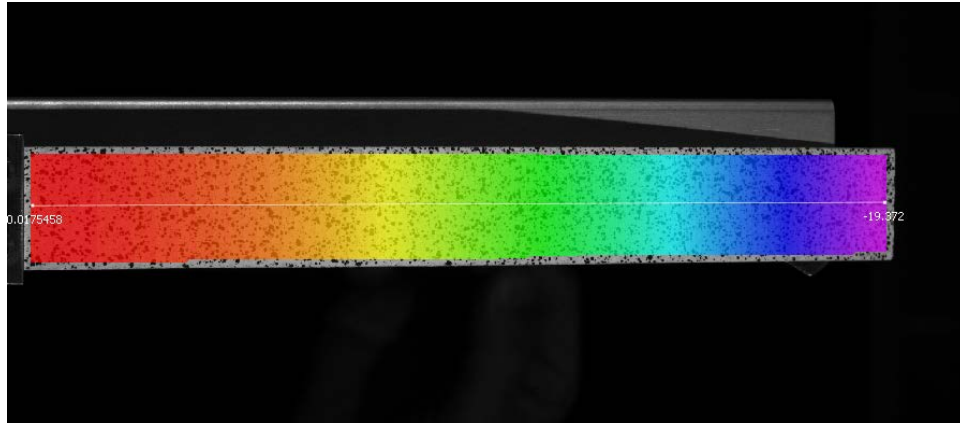


Figure 22. Point index line for measuring displacement along the centerline of the beam with 100 evenly spaced points

2. Experimental Natural Frequency of Cantilever Beam

The images taken by the HSC were used to determine the experimental natural frequency of the vibrating beams. This was accomplished by measuring the period of oscillations between frames as shown in Figure 23. The image on the left represents the beginning of the period and the image on the right represents the end of the period. The time was measured as a function of the frame rate then placed into Equation 3.7 to calculate the damped natural frequency. Multiple periods were determined for each beam to improve the accuracy.

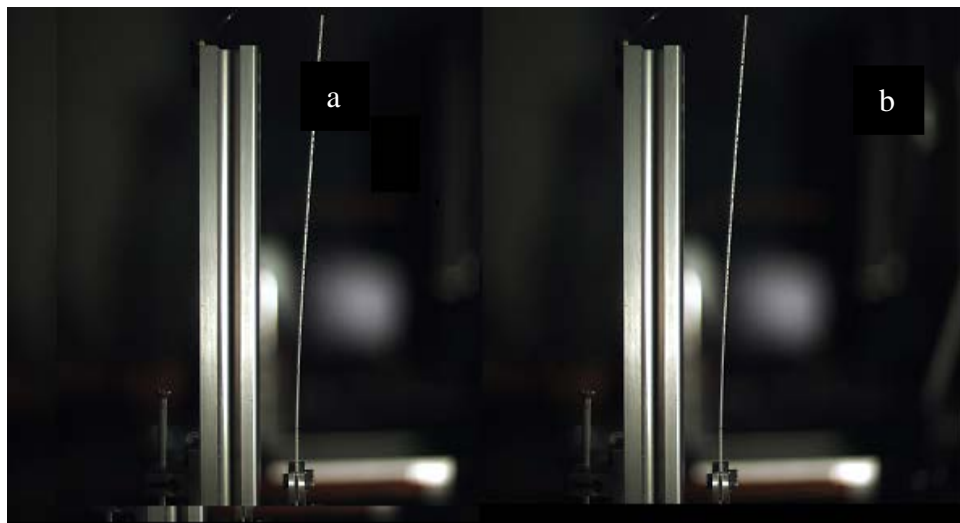


Figure 23. Determination of the period of oscillation using HSC images. (a) First free vibration peak at 0.2228 seconds. (b) Second free vibration peak at 0.2982 seconds

The experimental damping ratio was determined using:

$$\zeta = \frac{\frac{1}{n-1} \ln \left(\frac{x_1}{x_n} \right)}{\sqrt{4\pi^2 + \left[\frac{1}{n-1} \ln \left(\frac{x_1}{x_n} \right) \right]^2}} \quad (6.1)$$

The amplitudes for x_1 and x_n were extracted from the response at the tip of the beam as represented in Figure 24. The natural frequency was calculated using Equation 3.14. Tables 8–9 provide an overview of the theoretical and experimental fundamental frequencies of each beam in the air and water environments, respectively. Figures 25 and 26 are plots of the frequency distributions for each case.

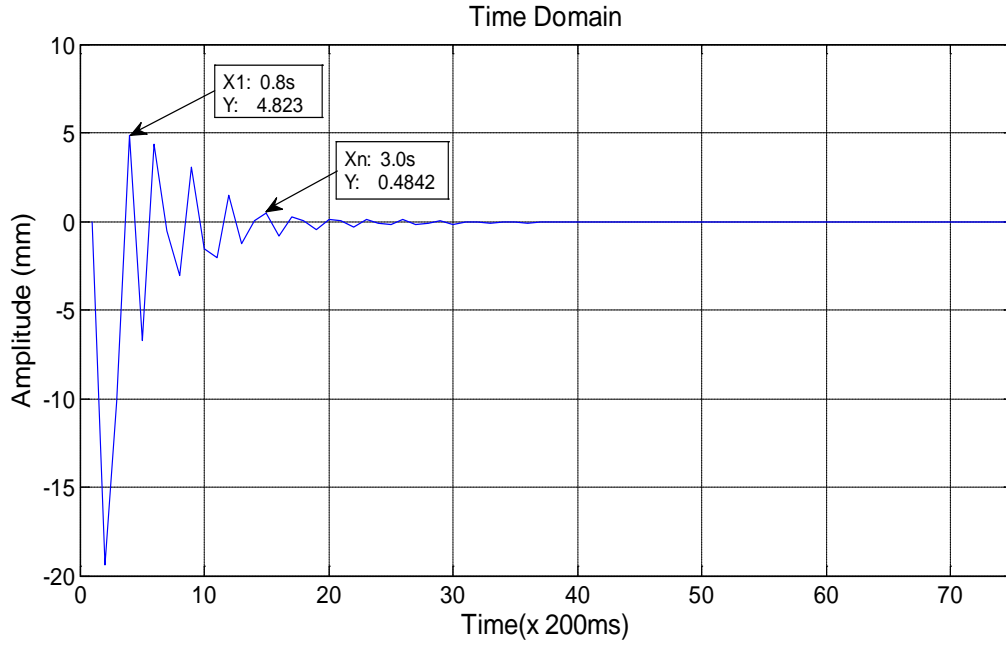


Figure 24. Representative sample of tip displacement as a function of time for the determination of damping

Table 8. Theoretical and experimental fundamental frequencies of each cantilever beam in air

Sample #	Orientation	Theoretical	Experimental				Error (%)
		f_n (Hz)	T (s)	f_d (Hz)	ζ	f_n (Hz)	
I	0°/90°	13.49	0.076	13.16	0.185599	13.39	0.74
	+/-45°	11.61	0.082	12.16	0.110203	12.24	5.40
II	0°/90°	13.59	0.075	13.29	0.156948	13.46	0.95
	+/-45°	11.44	0.090	11.08	0.293841	11.60	1.36
III	0°/90°	13.57	0.075	13.26	0.164041	13.44	0.98
	+/-45°	11.62	0.089	11.26	0.278209	11.73	0.92
IV	0°/90°	13.53	0.076	13.12	0.230972	13.48	0.34
	+/-45°	11.68	0.088	11.39	0.243061	11.74	0.56
V	0°/90°	13.46	0.075	13.27	0.119219	13.37	0.67
	+/-45°	11.54	0.088	11.39	0.213408	11.66	1.05

Table 9. Theoretical and experimental fundamental frequencies of each cantilever beam in water

Sample #	Orientation	T (s)	f_d (Hz)	ζ	f_n (Hz)
I	0°/90°	0.260	3.85	0.650173	5.07
	+/-45°	0.272	3.68	0.041043	3.69
II	0°/90°	0.246	4.09	0.688404	5.63
	+/-45°	0.298	3.37	0.039909	3.38
III	0°/90°	0.260	3.87	0.591436	4.80
	+/-45°	0.300	3.35	0.047513	3.35
IV	0°/90°	0.261	3.85	0.59128	4.77
	+/-45°	0.294	3.43	0.41715	3.77
V	0°/90°	0.254	3.97	0.402001	4.33
	+/-45°	0.286	3.57	0.297959	3.74

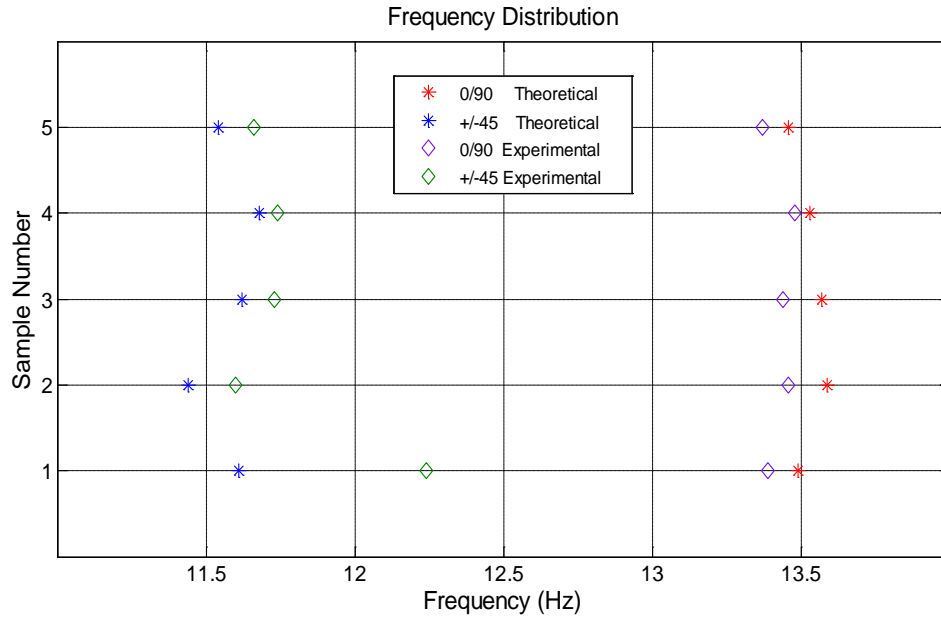


Figure 25. Fundamental frequency distribution for each cantilever beam in air environment with theoretical frequencies

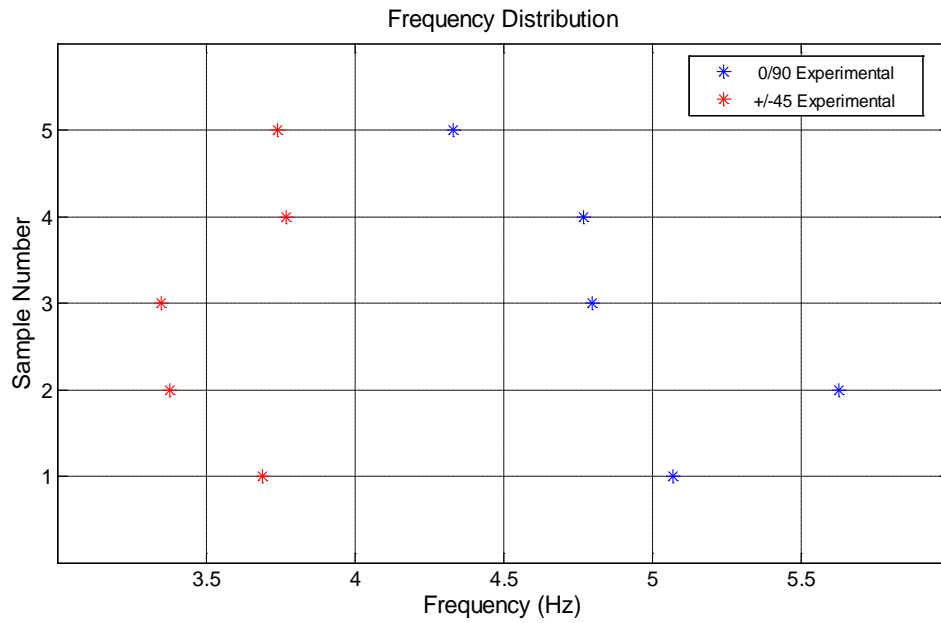


Figure 26. Fundamental frequency distribution for each cantilever beam in water environment

The theoretical values for natural frequency listed in Table 7 were calculated as a discrete system (Equation 5.6) using the exact dimensions of each beam. These values

are in good agreement with the obtained experimental natural frequencies with the exception of Sample I of $\pm 45^\circ$ orientation which has a large error. Visual inspection of the sample did not reveal any manufacturing abnormalities in the composite, so this error is likely due to human error. The average natural frequencies for the $0^\circ/90^\circ$ and $\pm 45^\circ$ orientations are 13.43 Hz and 11.68 Hz with average errors of 0.73% and 0.9%, respectively. Sample I of $\pm 45^\circ$ was not used in the average due to questionable data. The frequency is lowest in the $\pm 45^\circ$ samples, which is expected due to the decreased bending stiffness. However, with the exception of Sample I, the damping ratio was consistently higher in the $\pm 45^\circ$ samples.

For the tests conducted in water, the average natural frequencies for the $0^\circ/90^\circ$ and $\pm 45^\circ$ samples are 4.92 Hz and 3.58 Hz, respectively. The $\pm 45^\circ$ samples again showed lower frequencies than the $0^\circ/90^\circ$ samples. In contrast, the damping ratio was consistently lower in the $\pm 45^\circ$ samples. Given the much less harmonic motion of the beam in the data, it was much more difficult to calculate damping in Samples I, II, and III of $\pm 45^\circ$ orientation. Thus, the damping for these samples is questionable.

The natural frequencies for the beams when tested in air are much higher than when tested in water. This is expected due to the added mass effect in FSI. On average, the added mass effect on the beams in a water environment decreases its natural frequency by 3.1 times those seen in an air environment. However, this may be slightly skewed since the damping in Samples I, II, and III of $\pm 45^\circ$ orientation is questionable. Nonetheless, the values listed are relevant given that damping has little effect on the natural frequency.

3. Free Vibration Response

Since a system under free vibration will vibrate at one or more of its natural frequencies, its response shape is described as the linear combination of mode shapes. In other words, the shape of which the beam takes on at an instance of time is seen as the weighted sum of all mode shapes. Each natural frequency corresponds to a specific mode shape. Figure 27 depicts the first three theoretical mode shapes of a cantilever beam under free vibration.

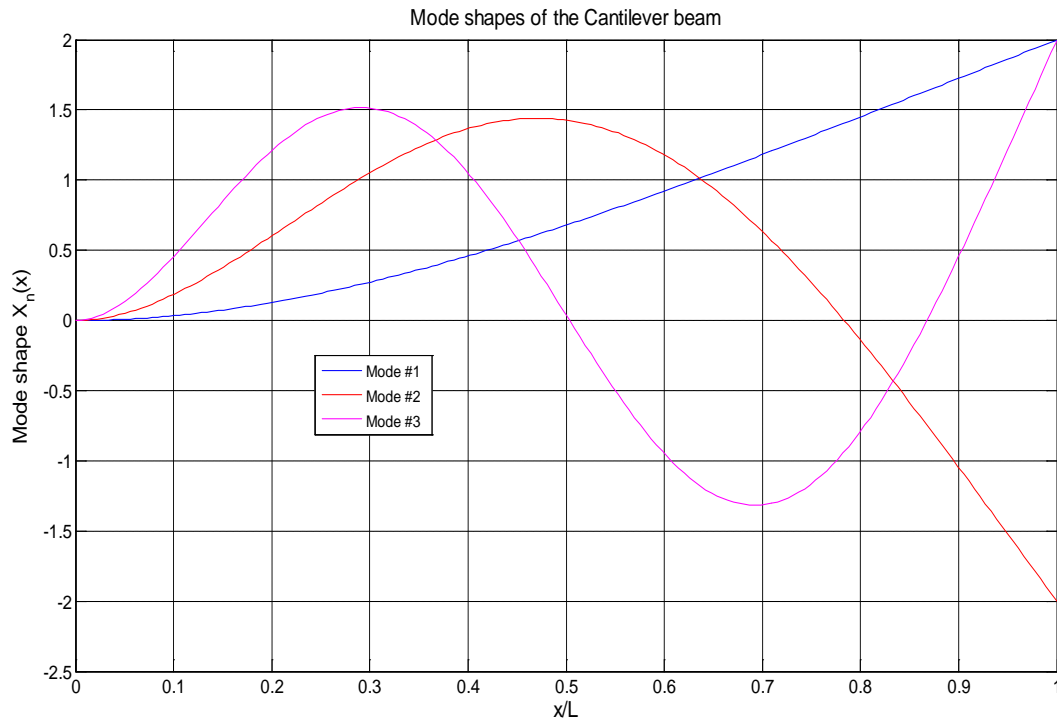


Figure 27. Theoretical displacement configuration of Modes I, II, and III for a cantilever beam under free vibration

Since the initial displacement of the beam closely resembles the Mode I shape, it is reasonable to expect that this shape will dominate the structure in its free vibration response shape. Figures 28 through 31 are the free vibration response shapes for representative samples in air and in water. Specifically, Sample V of $0^\circ/90^\circ$ and Sample III of $\pm 45^\circ$ are selected. Each line in the graphs is representative of the displacement along the length of the beam. The top graph in each figure corresponds to the first couple of seconds where the beam is in free vibration. The bottom graph corresponds to the remaining recorded time in two second intervals. The full set of free vibration response shape plots are in Appendix B for tests conducted in air and Appendix C for tests conducted in water.

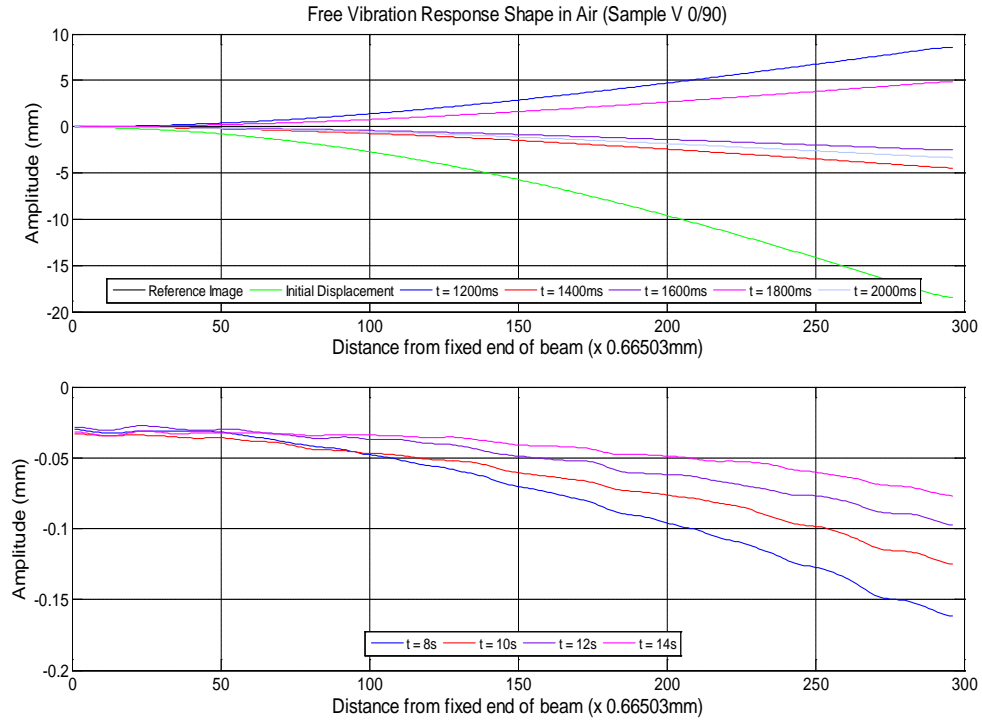


Figure 28. Free vibration response shape in air at various times for Sample V of $0^{\circ}/90^{\circ}$ orientation

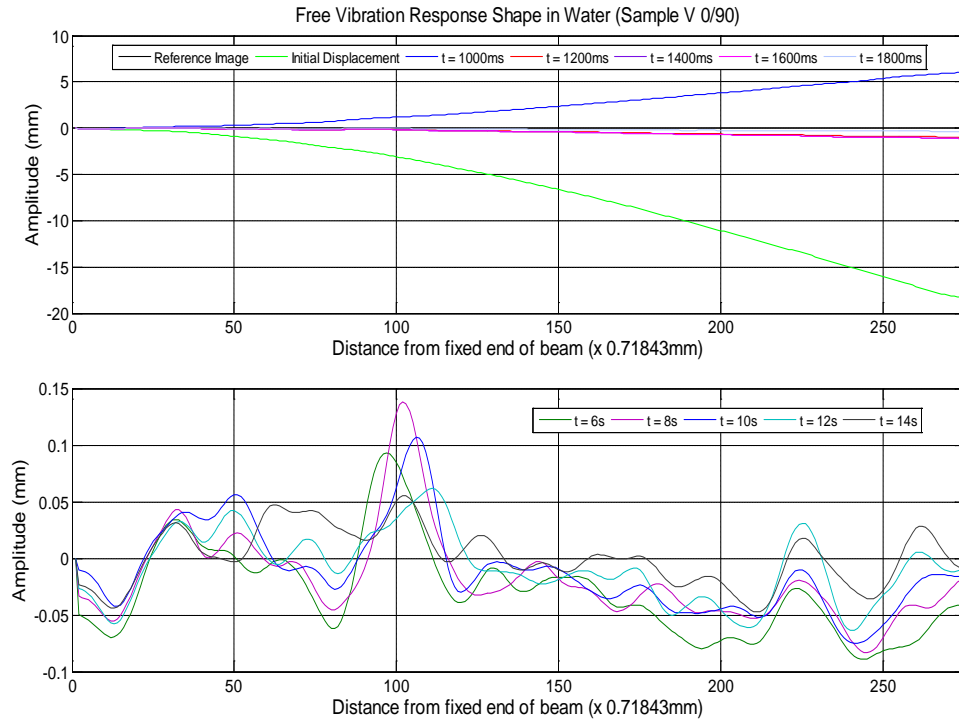


Figure 29. Free vibration response shape in water at various times for Sample V of $0^{\circ}/90^{\circ}$ orientation

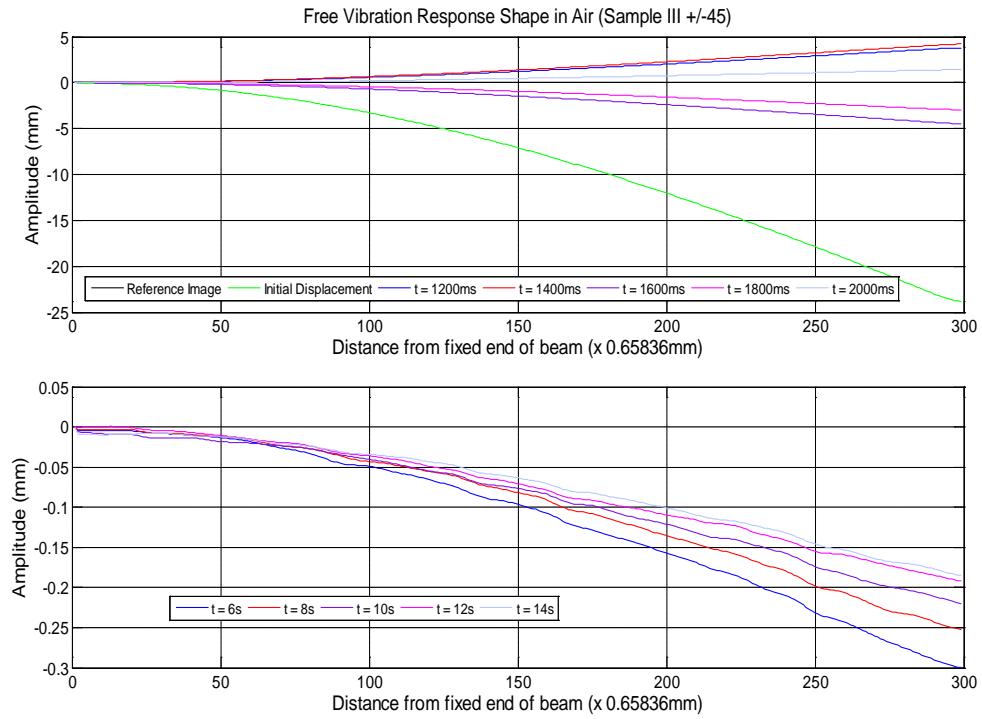


Figure 30. Free vibration response shape in air at various times for Sample III of $\pm 45^\circ$ orientation

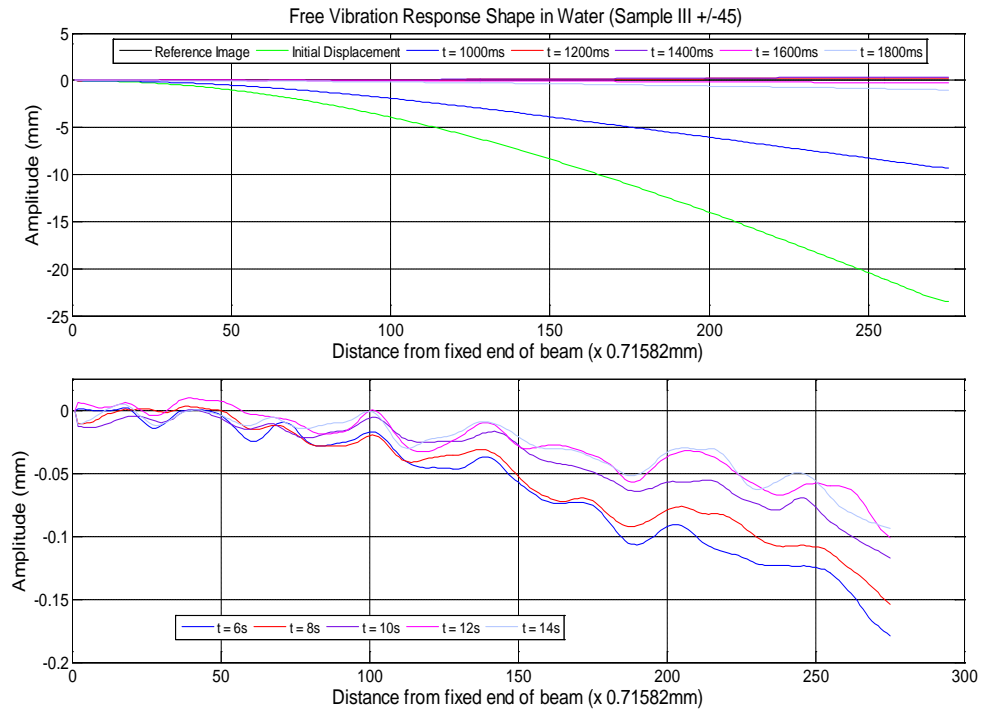


Figure 31. Free vibration response shape in water at various times for Sample III of $\pm 45^\circ$ orientation

It is apparent that Mode I is the dominant shape for the first couple of seconds in the free vibration in Figures 28 through 31. As time progresses, the response shape of Sample V in air (Figure 28) remains relatively the same. There are some ripples present but this is probably caused by noise in the system. In water, however, the result is much different. The graph shows multiple smaller peaks with four larger, distinct peaks at the various times. The response shape appears to remain the same throughout the test period, leading to the conclusion that this phenomenon is just the surface characteristics of the composite beam magnified by the water since the DIC method only measures deformation on the surface of an object and not through its thickness. However, this could be due to a synchronization of the time interval in which images are captured with the period of the vibration; but the use of low speed cameras cannot achieve the optimal sampling rate to prove this theory.

Figure 32 and Figure 33 are three-dimensional representations of reference image of the composite beam in air and water. These representations show the surface characteristics of the beam with all displacements at zero, in which both are exactly the same. It is from these reference images that all other displacements are measured. Figures 34 through 36 are provided as other visualizations of the free response shapes at various times. Specifically, Figure 34 is a depiction of the test in air of Sample V. It shows a smooth transition throughout the contours just as it is presented in Figure 28. The displacements along the beam of Sample V at 2400 ms in water are shown in Figure 35 and Figure 36, respectively.

Sample III of $\pm 45^\circ$ orientation shows the same type of phenomenon as shown in Figures 30 and 31, though the displacement peaks are much less pronounced in the sample when tested in water. This is likely due to the layer orientation of the composite. The effect of FSI in each water test was readily apparent in all of the samples, but showed less of an effect on the $\pm 45^\circ$ orientation samples as compared to the $0^\circ/90^\circ$ samples. This is consistent throughout all of the samples tested. This leads to one of two conclusions:

- The FSI effect creates a different linear combination of mode shapes in water than in air.
- The FSI effect changes the individual mode shapes when in water than in air.

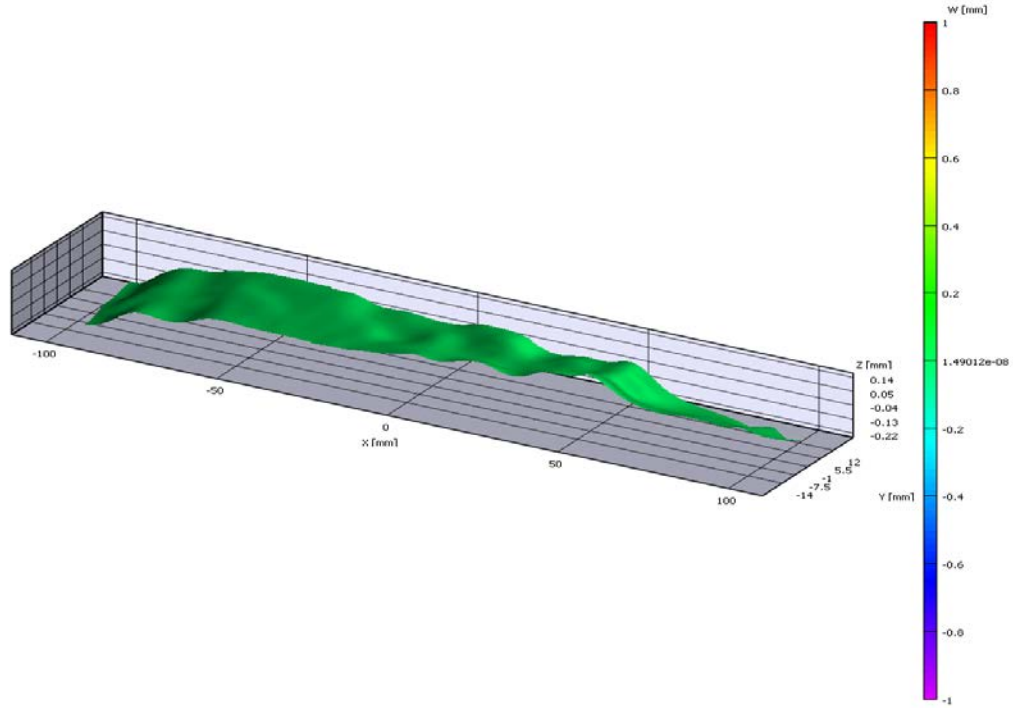


Figure 32. Three-dimensional representation of the reference image used for correlation in air for Sample V of $0^\circ/90^\circ$ orientation

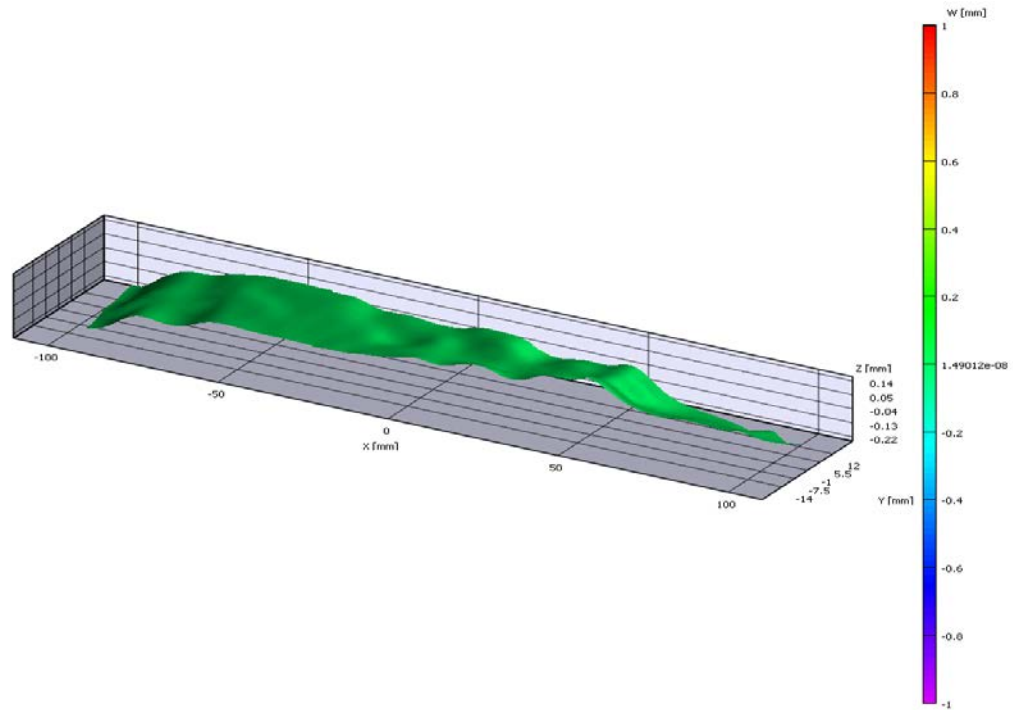


Figure 33. Three-dimensional representation of the reference image used for correlation in water for Sample V of $0^\circ/90^\circ$ orientation

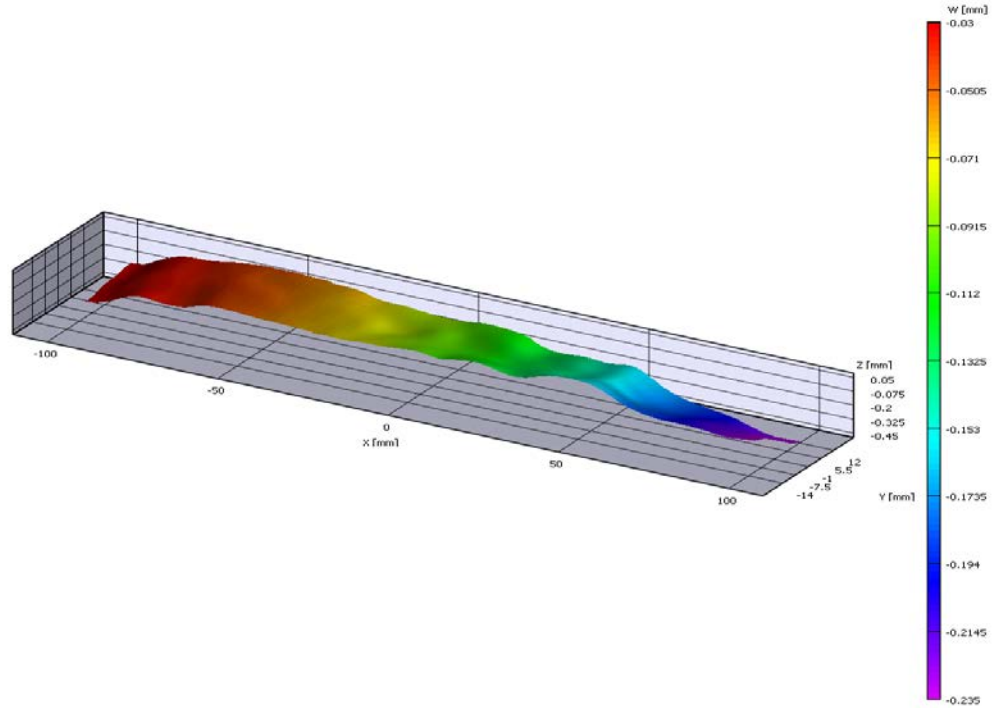


Figure 34. Three-dimensional representation of the free vibration response shape at 6000 ms after the initial displacement in air for Sample V of $0^\circ/90^\circ$ orientation

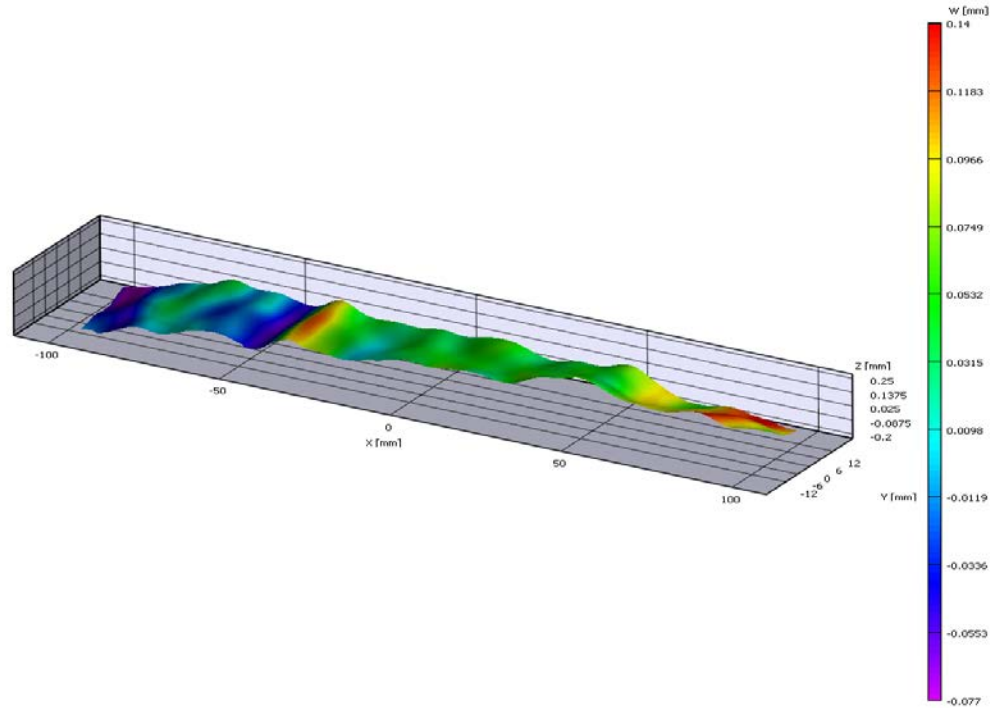


Figure 35. Three-dimensional representation of the free vibration response shape at 2400 ms after initial displacement in water for Sample V of $0^\circ/90^\circ$

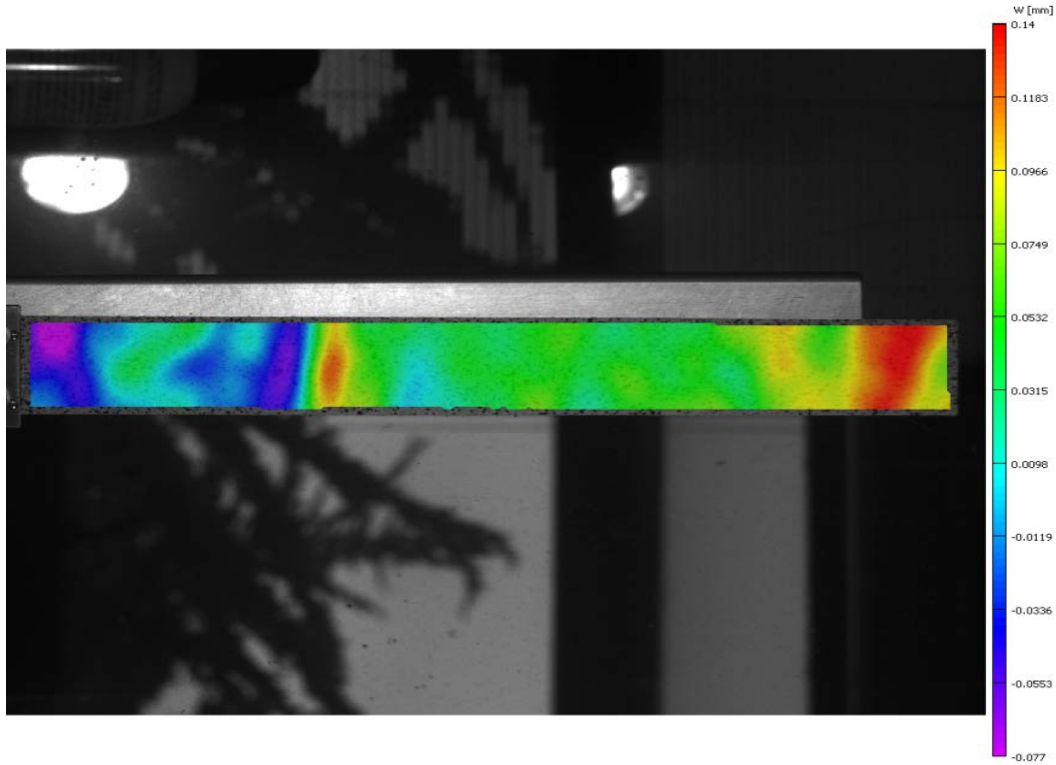


Figure 36. Contour plot overlay of displacements along the length of the cantilever beam in water at 2400 ms after initial displacement for Sample V of $0^{\circ}/90^{\circ}$ orientation

B. IMPACT HAMMER TEST

1. Experimental Natural Frequency of the Free-Free Beam

Due to complications with the accelerometers, the composite beam with $\pm 45^{\circ}$ orientation was not tested. The results and analysis of the composite beam of $0^{\circ}/90^{\circ}$ orientation is contained herein. Tables 10 and 11 provide an overview of the theoretical and experimental natural frequencies for each mode of the free-free beams of each type in air and water environments, respectively. Figures 37 and 38 are the frequency distributions for each case.

Table 10. Theoretical and experimental natural frequencies of the free-free composite beam of $0^\circ/90^\circ$ orientation and aluminum beam in air

	Mode	Natural Frequency (Hz)		ζ	f_n	% error
		Theoretical	f_d			
Composite Beam $0^\circ/90^\circ$	1	52.88	51.4	0.0454	52.93	0.103
	2	145.75	143	0.0348	145.84	0.061
	3	285.71	272	0.0339	285.87	0.058
Al Beam	1	144.66	142	0.0083	144.66	0.001
	2	398.75	389	0.00924	398.77	0.003
	3	781.65	767	0.00465	781.66	0.057

Table 11. Experimental natural frequencies of the free-free composite beam of $0^\circ/90^\circ$ orientation and aluminum beam in water

Mode	f_n (Hz)
1	29.5
2	162
3	261

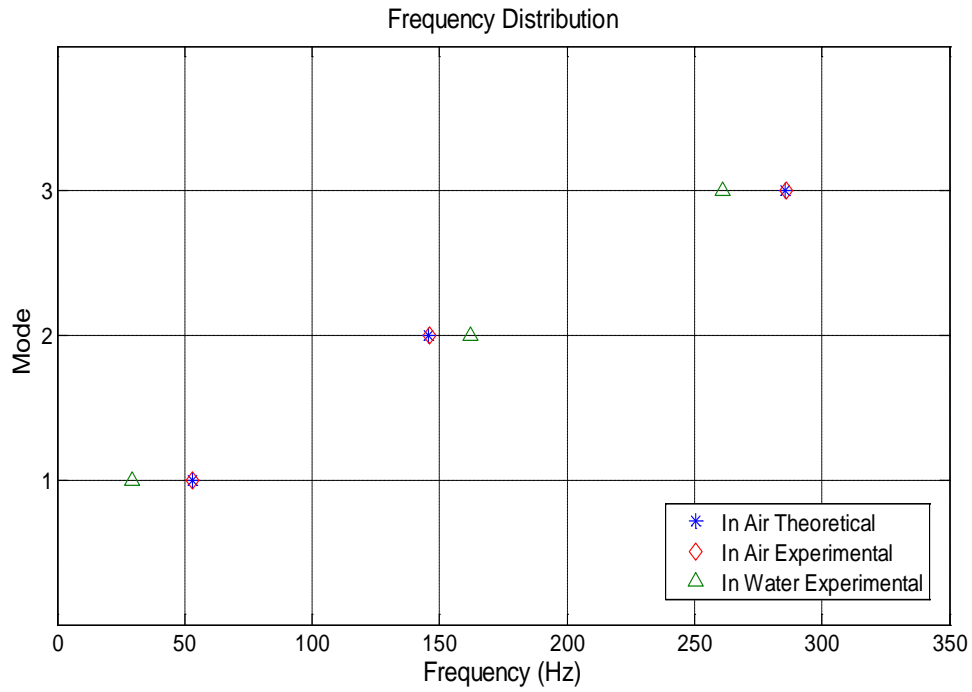


Figure 37. Frequency distribution for Modes I, II, and III of free-free composite beam of $0^\circ/90^\circ$ orientation beams in air and water environments

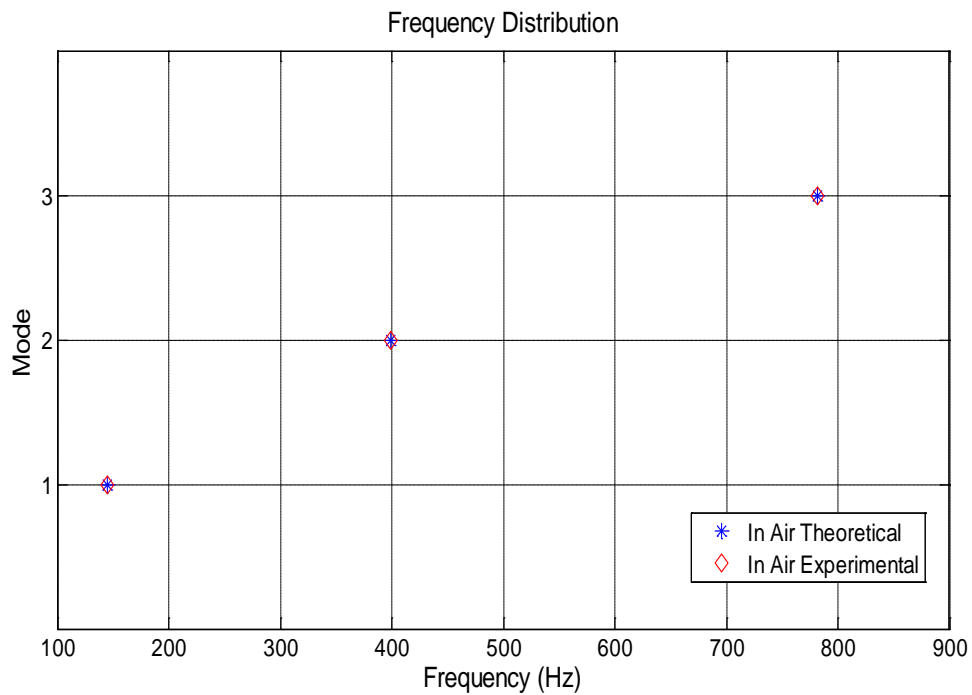


Figure 38. Frequency distribution for Modes I, II, and III of free-free aluminum beam in air and water environment with theoretical frequencies

The theoretical values for natural frequency listed in Table 10 were calculated using Equation 5.11 with the exact dimensions of each beam. These values are in good agreement with the obtained experimental natural frequencies for each mode. Unlike the natural frequencies found in the DIC tests, the natural frequencies of each mode in the impact hammer test did not decrease by one-third. This may be due to the differing stiffness's and/ or boundary conditions of the composite beams in the two tests. The natural frequency associated with Mode I of the free-free composite beam decreased by a half when tested in water. However, the natural frequency associated with Mode II increased by approximately 16 Hz when tested in water. The second mode shape in water (Figure 44) is more similar to the third mode shape in air (Figure 42) rather than the second mode shape in air (Figure 41). Therefore, the second frequency in water should be compared to the third frequency in air. Such a comparison is also indicative of reduction in half in the second natural frequency with the added mass.

2. Mode Shape Comparison of the Composite Beam

Figure 39 is the theoretical mode shapes for the first three modes of a free-free beam. Figures 40 through 42 are illustrations of the mode shapes at the natural frequencies of the free-free composite beam in air. These are the baseline for comparison with its mode shapes at its natural frequencies in water as shown in Figures 43 through 45.

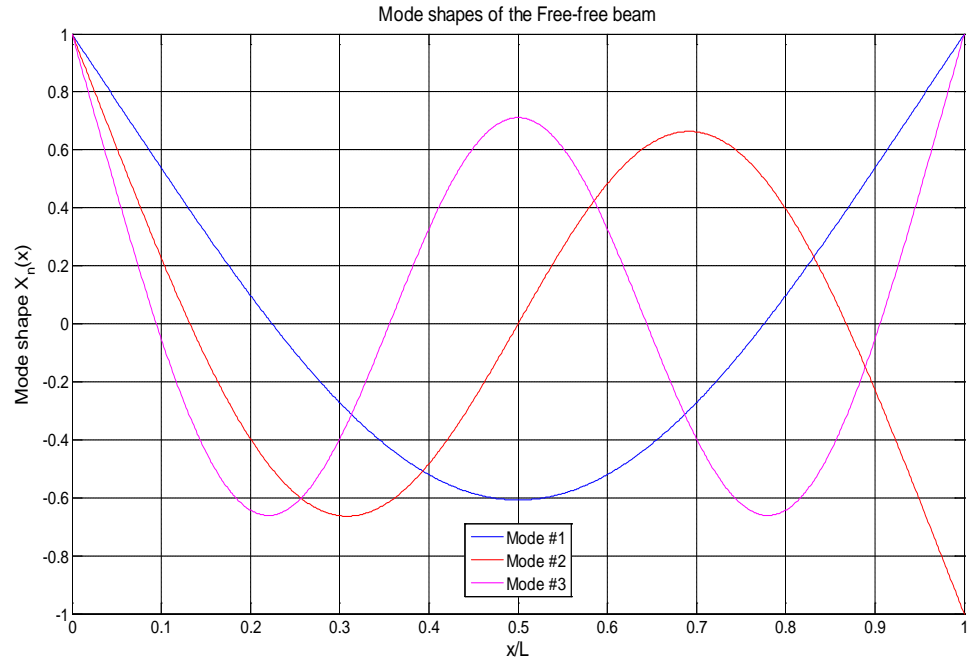


Figure 39. Theoretical mode shapes for Mode I, II, and III of a free-free beam

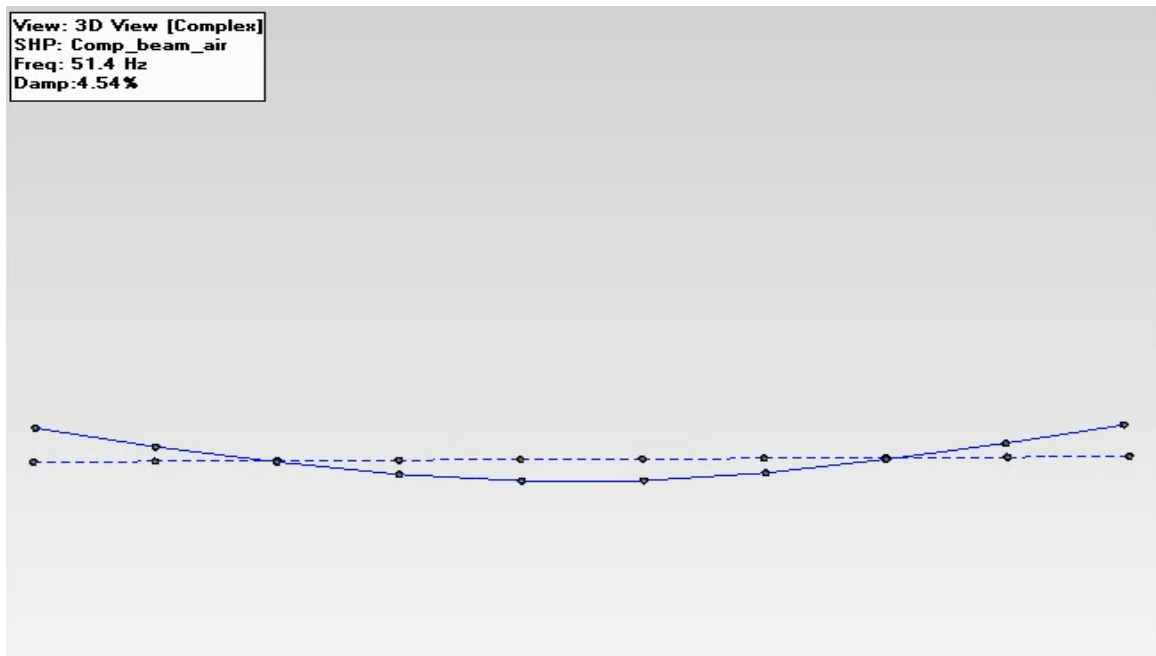


Figure 40. Mode I of free-free composite beam of $0^\circ/90^\circ$ orientation in air

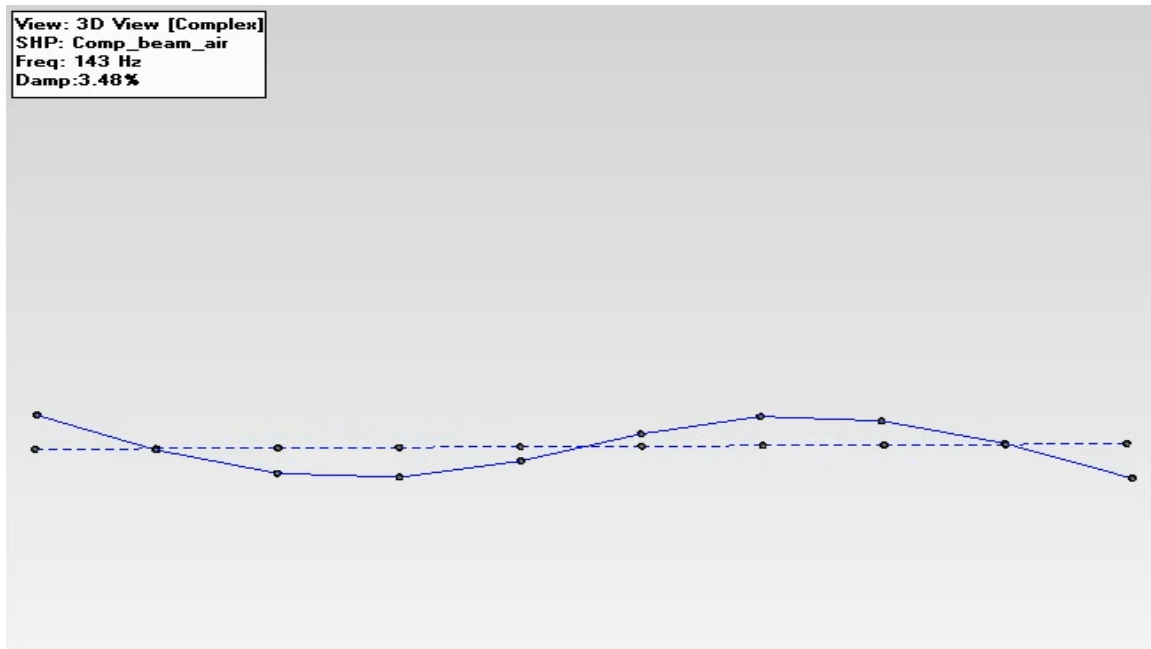


Figure 41. Mode II of free-free composite beam of $0^\circ/90^\circ$ orientation in air

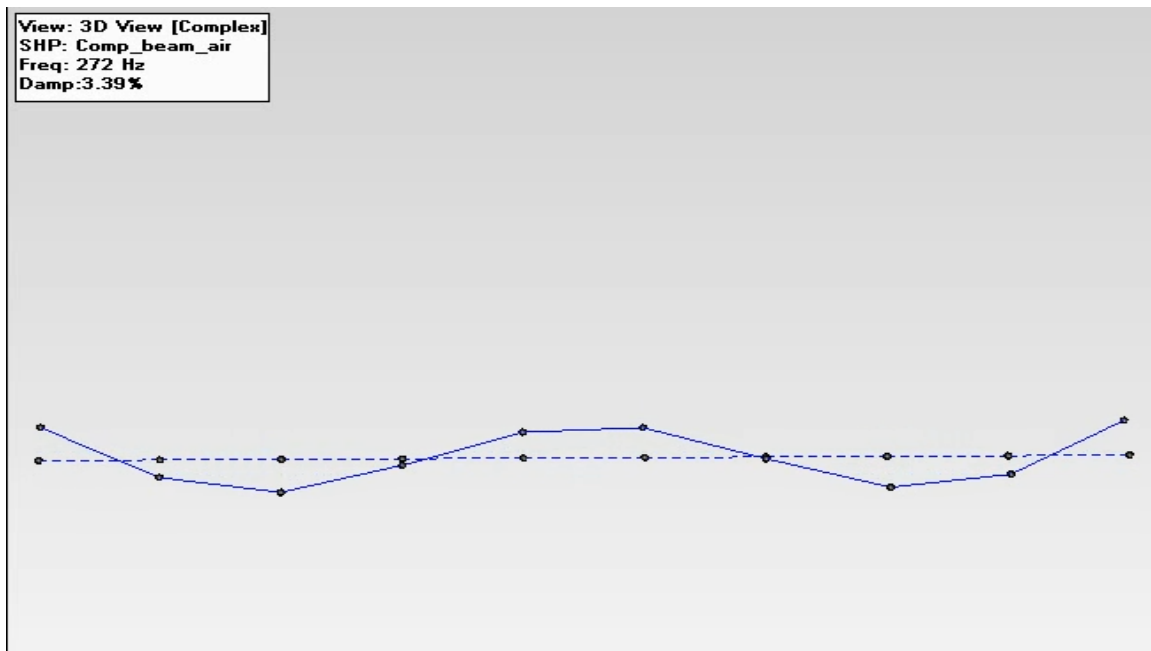


Figure 42. Mode III of free-free composite beam of $0^\circ/90^\circ$ orientation in air

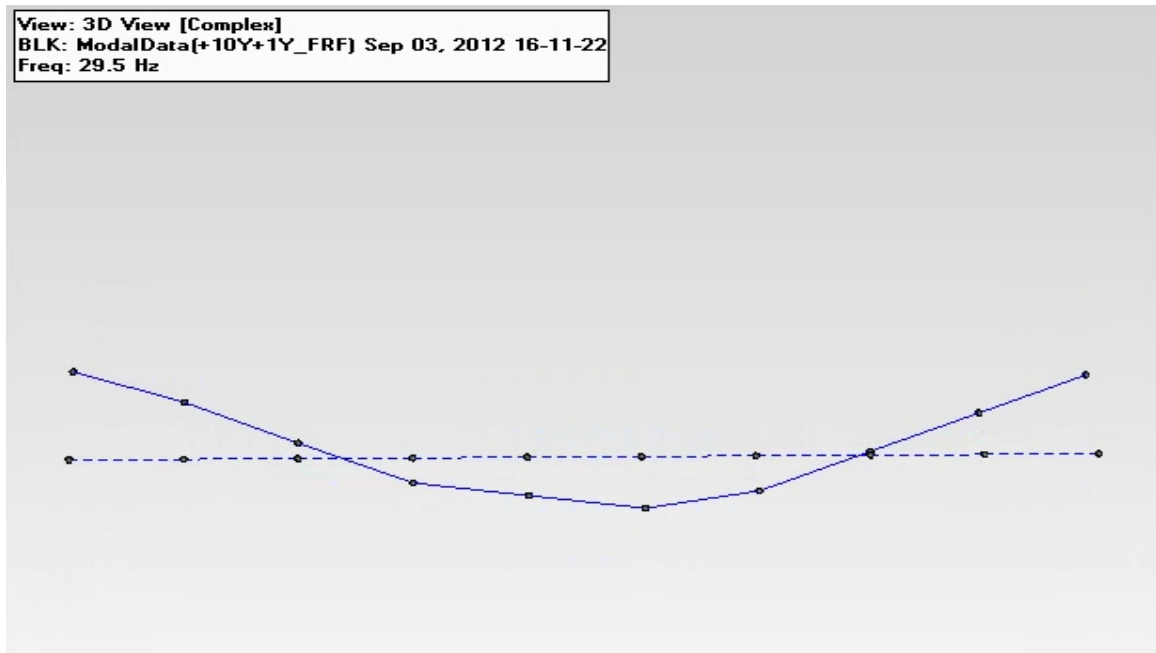


Figure 43. Mode I of free-free composite beam of $0^{\circ}/90^{\circ}$ orientation in water

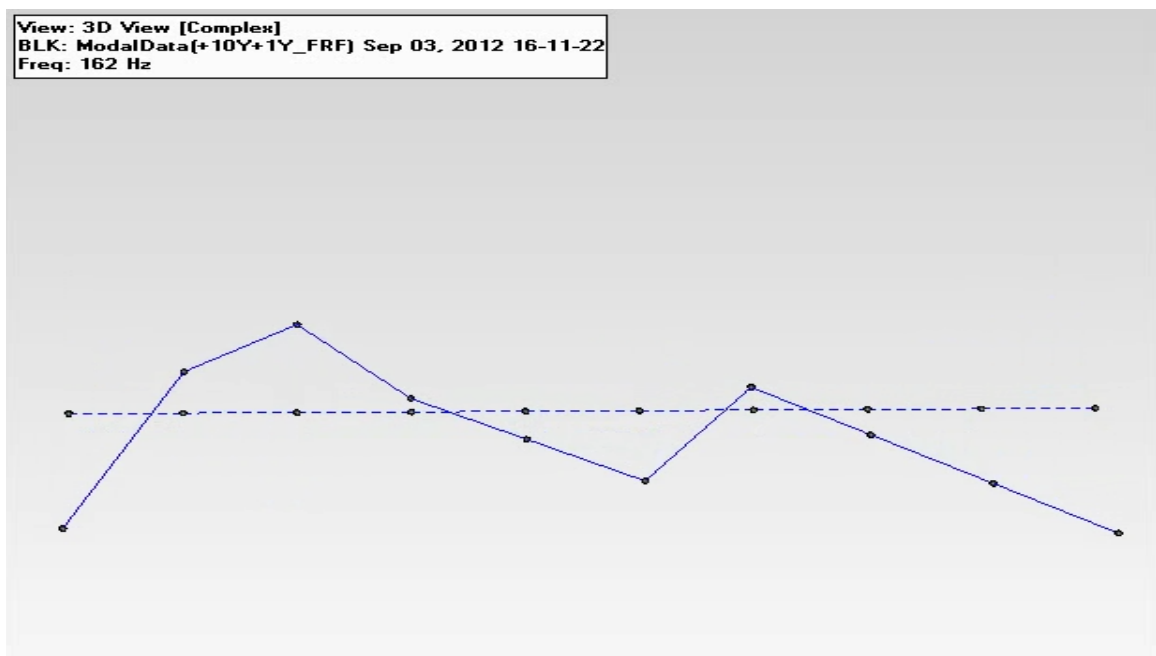


Figure 44. Mode II of free-free composite beam of $0^{\circ}/90^{\circ}$ orientation in water

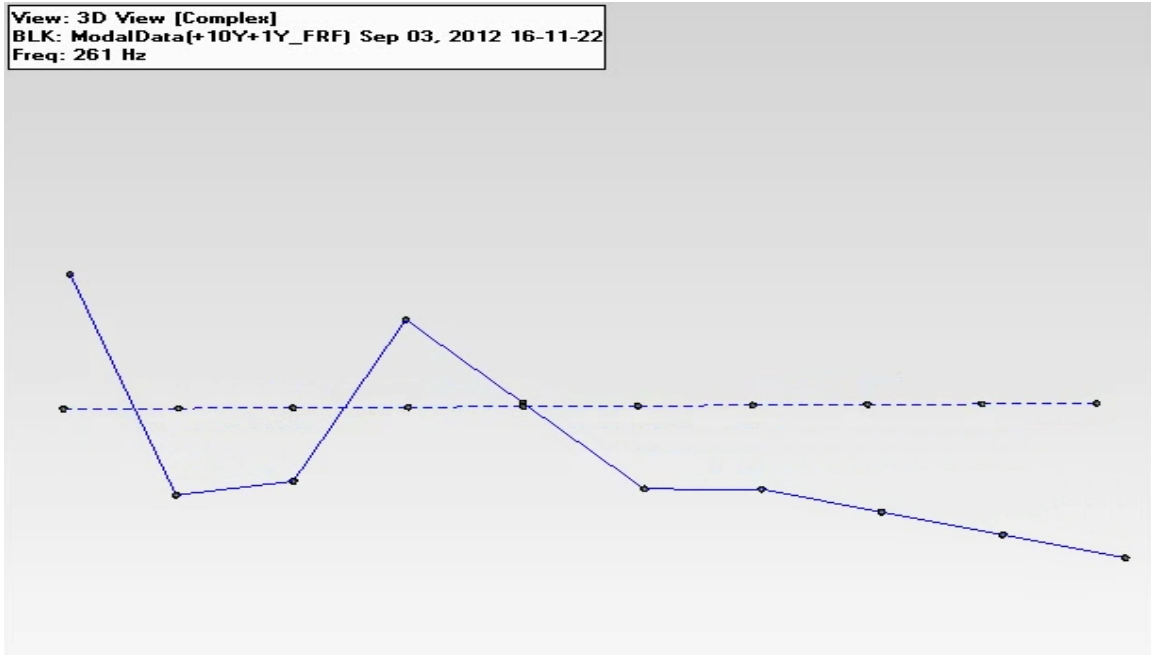


Figure 45. Mode III of free-free composite beam of $0^{\circ}/90^{\circ}$ orientation in water

The mode shapes for the composite beam in air (Figures 40 through 42) concur with the theoretical mode shapes in Figure 39. The mode shapes are symmetrical in appearance and contain the correct number of nodal points associated with each mode. For the tests conducted in water (Figures 43 through 45), the results are skewed. Accelerometers four, five, and eight were interpolated in order to view the mode shapes which was due to excessive noise in their signals. The Mode I shape is close to the mode shape in air but it does not contain a node on the left hand side of the beam. This becomes more evident when the mode shape is animated in the software program.

When animated, all three modes in the water tests only have one nodal point along the beam. The first four points on the right hand side of the beam in Figure 44 act as a rigid body in that they remain in a straight line relative to one another throughout oscillation. If Mode II did contain the four nodal points at the locations shown, it would actually represent Mode III for the system which would explain the increase in frequency by 16 Hz represented in Figure 37. Figure 45 contains questionable data and therefore is not conclusive in determining the shape of the beam at that mode and natural frequency.

In all cases where the beam was tested in water, it is appears that complex mode shapes are being excited which can be determined by looking at the phase relationships. A complete modal analysis is required for this.

VII. CONCLUSIONS AND RECOMENDATIONS

This study was conducted to gain a better understanding of composite materials that are similar to those used in marine applications under conditions in which FSI is occurring. A series of experiments were conducted to compare the dynamic response of composite beams in free vibration in air and water environments. The composite beams were constructed of 6 oz E-glass cloth with varying numbers of layers and orientations, and boundary conditions in order to provide the best possible test conditions for this study. These include cantilever beams with 6 layers oriented at $0^\circ/90^\circ$ and at $\pm 45^\circ$ as well as a free-free beam with 16-layers oriented at $0^\circ/90^\circ$.

The results of this study show how significant the added mass effect of FSI is on composites of similar density to water. On average, the frequencies of the cantilever beam decreased by one-third when submerged in water while the frequency of the free-free beam decreased by one half with the added mass. Additionally, it has been shown that the free vibrational mode shapes of the composite beams of $0^\circ/90^\circ$ orientation are different between in air tests and in water tests. The second mode shape in air does not exist in water. The results of this study also show that FSI appears to have less of an effect on the free vibration response shape of composites constructed with a $\pm 45^\circ$ layer orientation.

Numerous experimental tests have been conducted to study the dynamic responses of composite materials used in marine applications. This study will hopefully give additional insight into the significant effects FSI has on the free vibration response of composites being implemented into the structural design of U.S. Navy ships.

Though there are many areas of FSI to be studied, further studies should include using a shaker to characterize the modes shapes of vibrating composite structures while submerged in water and conducting a modal analysis on clamped composite plates with varying FSI conditions. Specifically, a modal analysis of a clamped plate resting on the

free surface of water would simulate similar conditions in which composites on ships would incur. Further, study of composites with FSI should include testing with variations in pressure, salinity, and temperature.

APPENDIX A: ACCELEROMETER PLACEMENTS

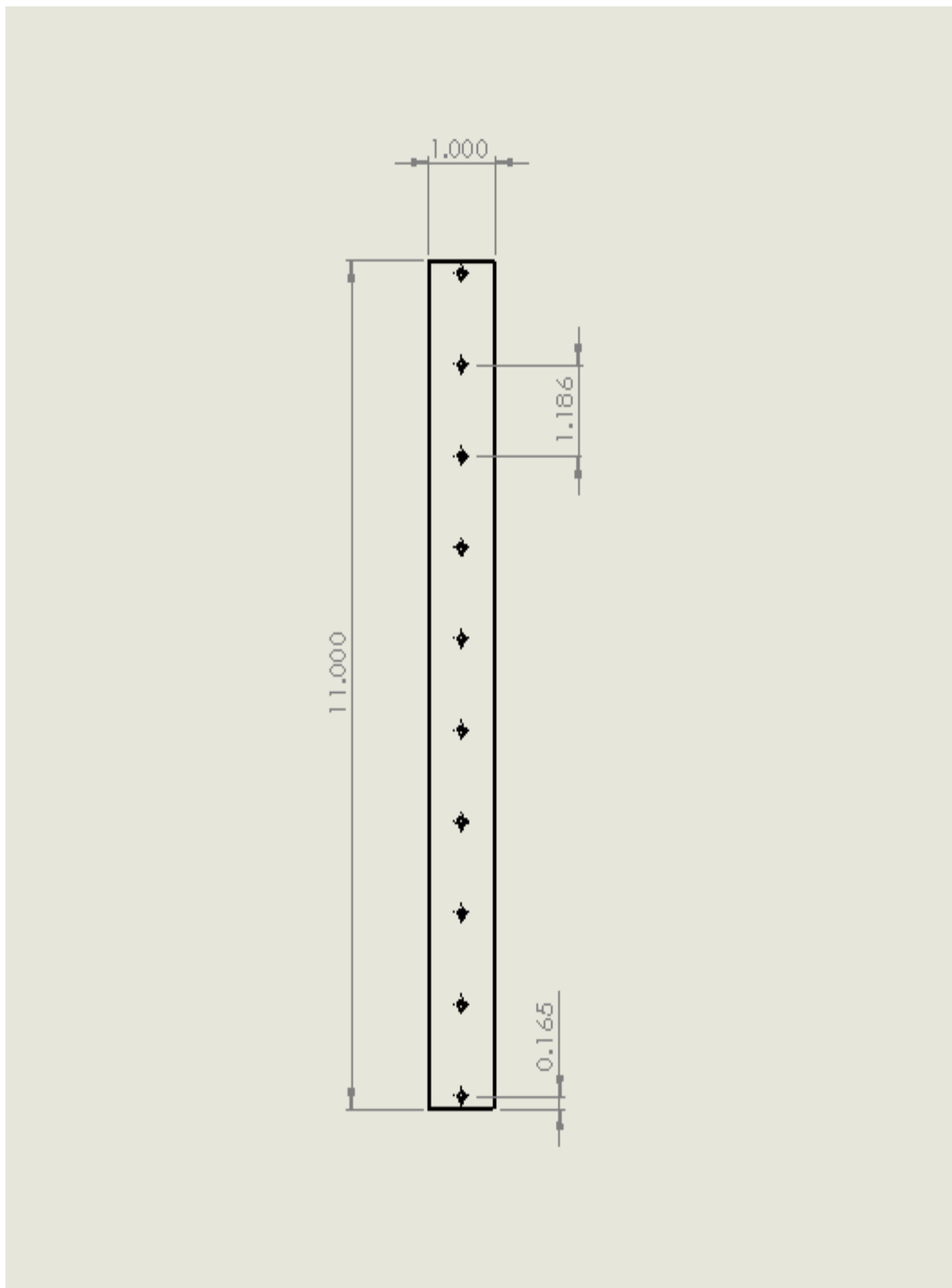


Figure 46. Composite beam with accelerometer placements

THIS PAGE INTENTIONALLY LEFT BLANK

APPENDIX B: FREE VIBRATION RESPONSE IN AIR PLOTS

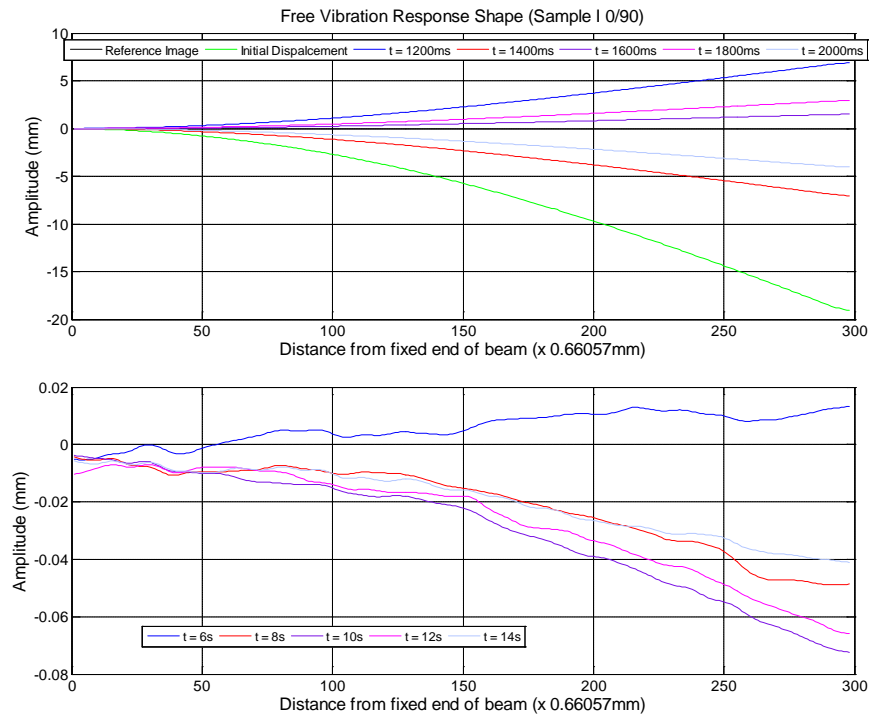


Figure 47. Free vibration response shape in air at various times for Sample I of 0°/90° orientation

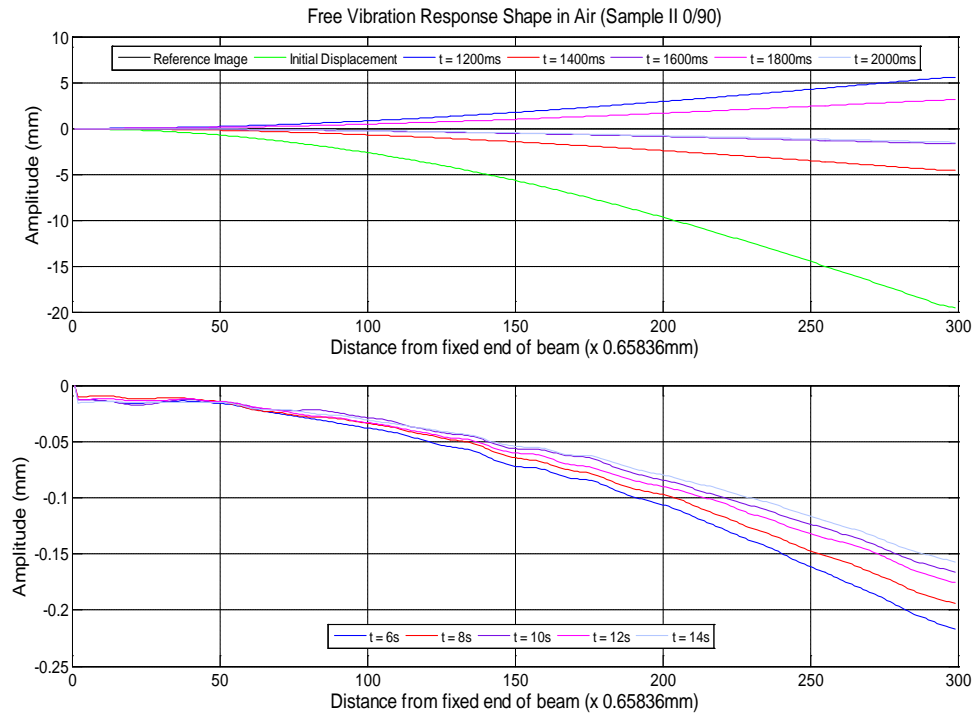


Figure 48. Free vibration response shape in air at various times for Sample II of $0^\circ/90^\circ$ orientation

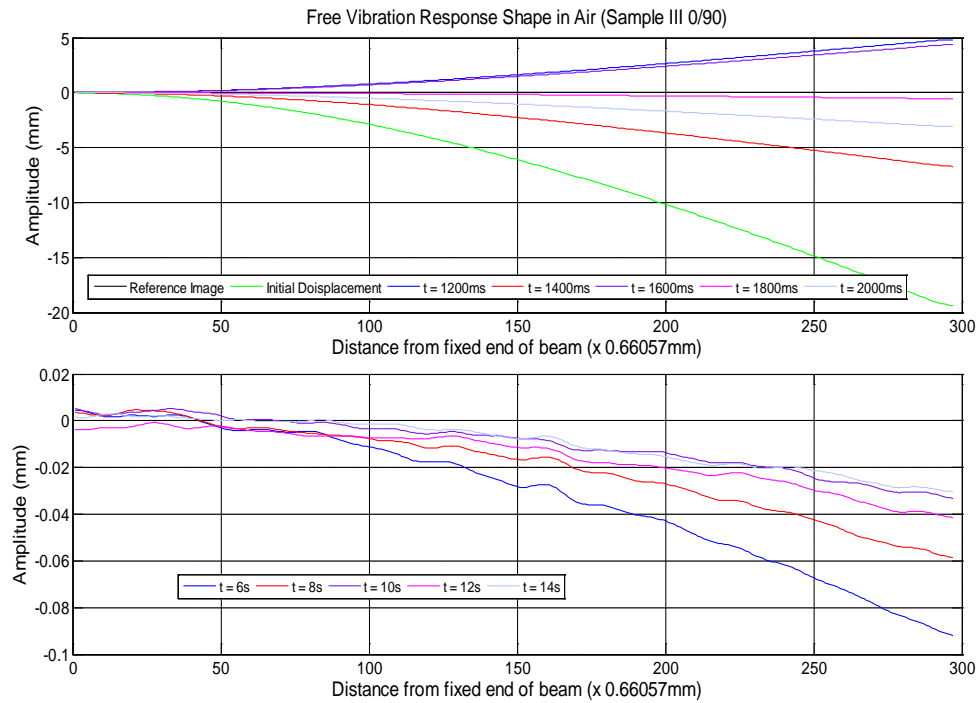


Figure 49. Free vibration response shape in air at various times for Sample III of $0^\circ/90^\circ$ orientation

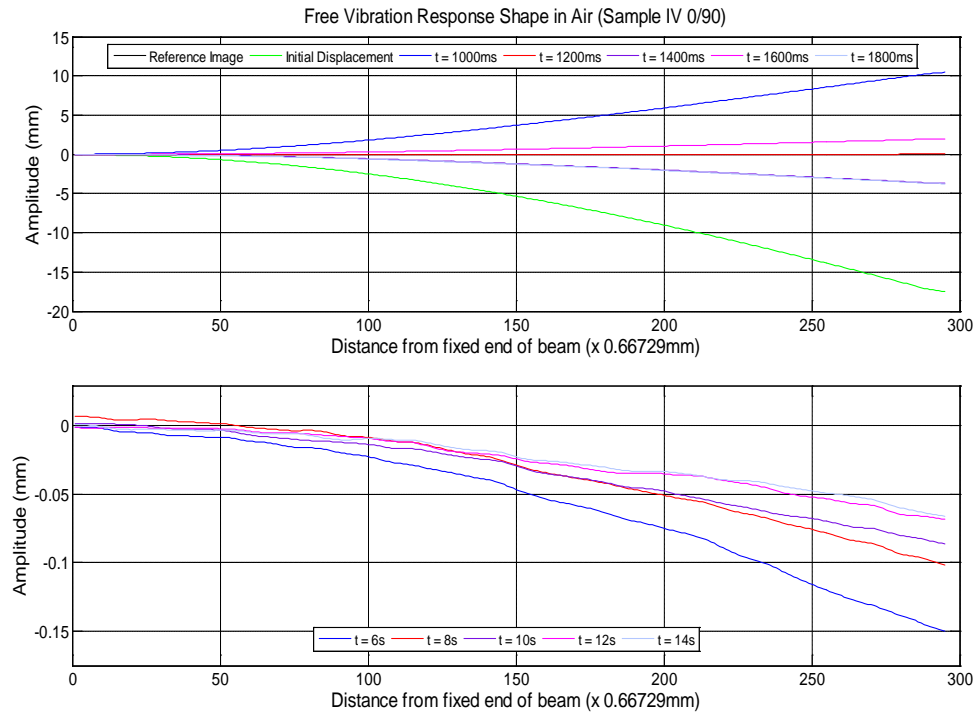


Figure 50. Free vibration response shape in air at various times for Sample IV of $0^\circ/90^\circ$ orientation

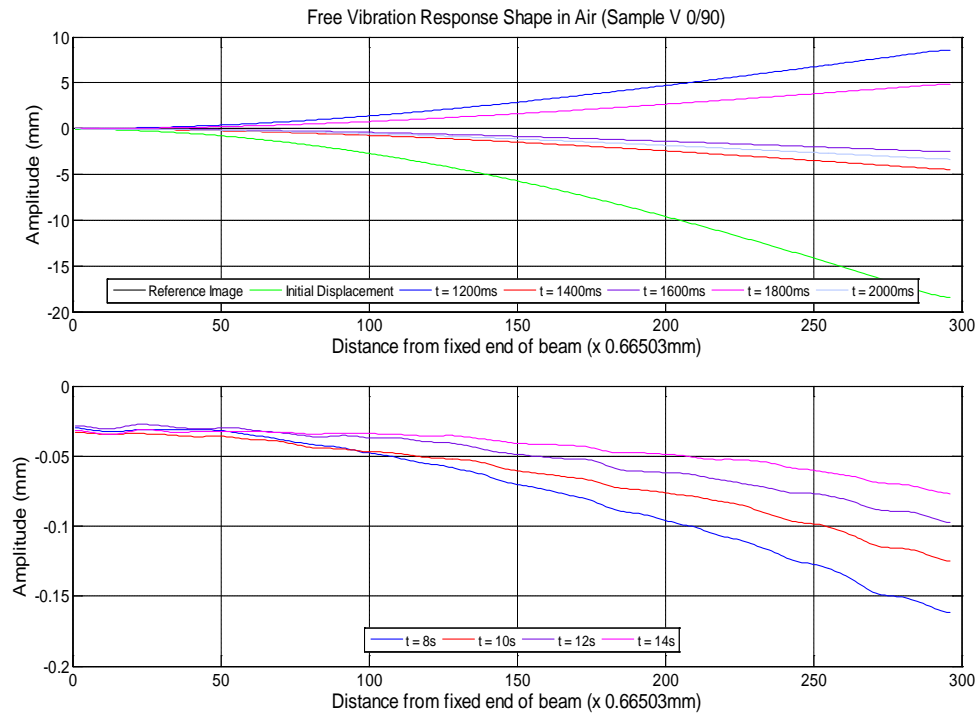


Figure 51. Free vibration response shape in air at various times for Sample V of $0^\circ/90^\circ$ orientation

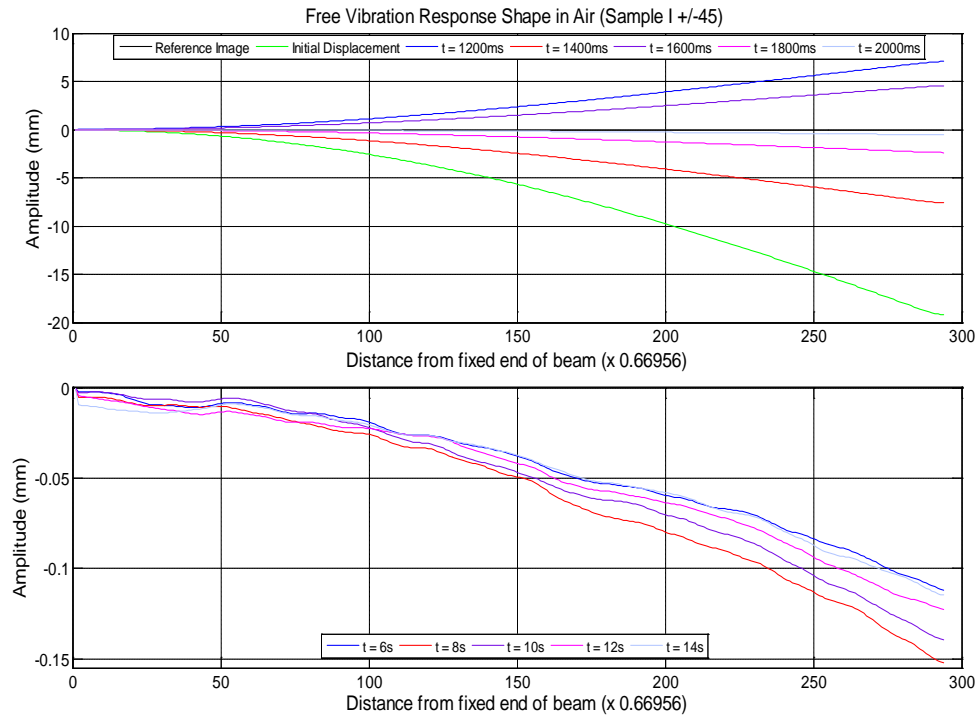


Figure 52. Free vibration response shape in air at various times for Sample I of $\pm 45^\circ$ orientation

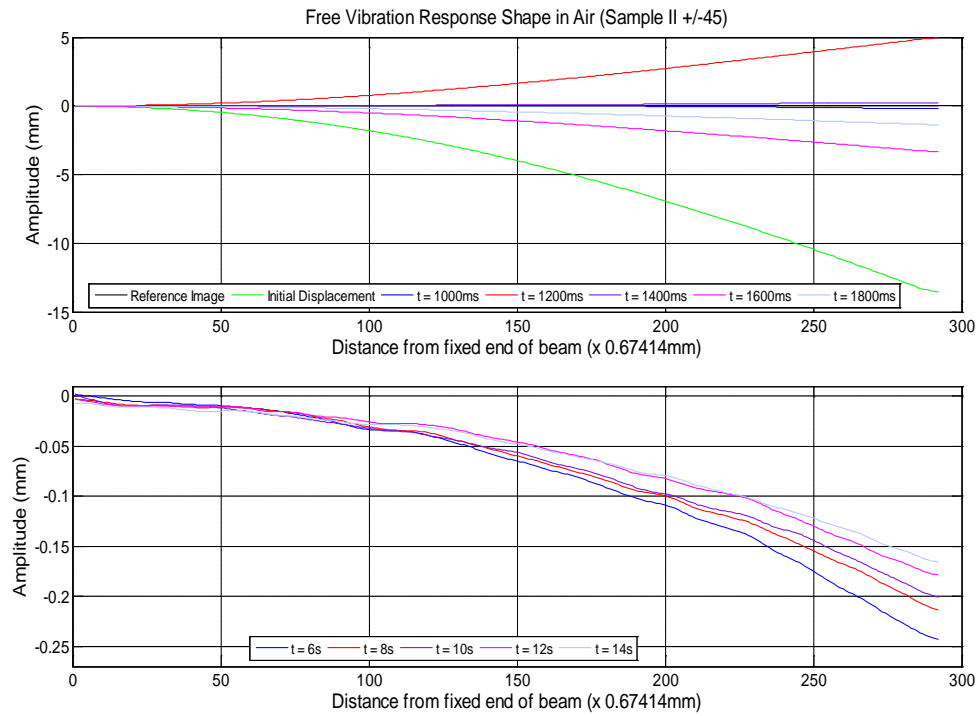


Figure 53. Free vibration response shape in air at various times for Sample II of $\pm 45^\circ$ orientation

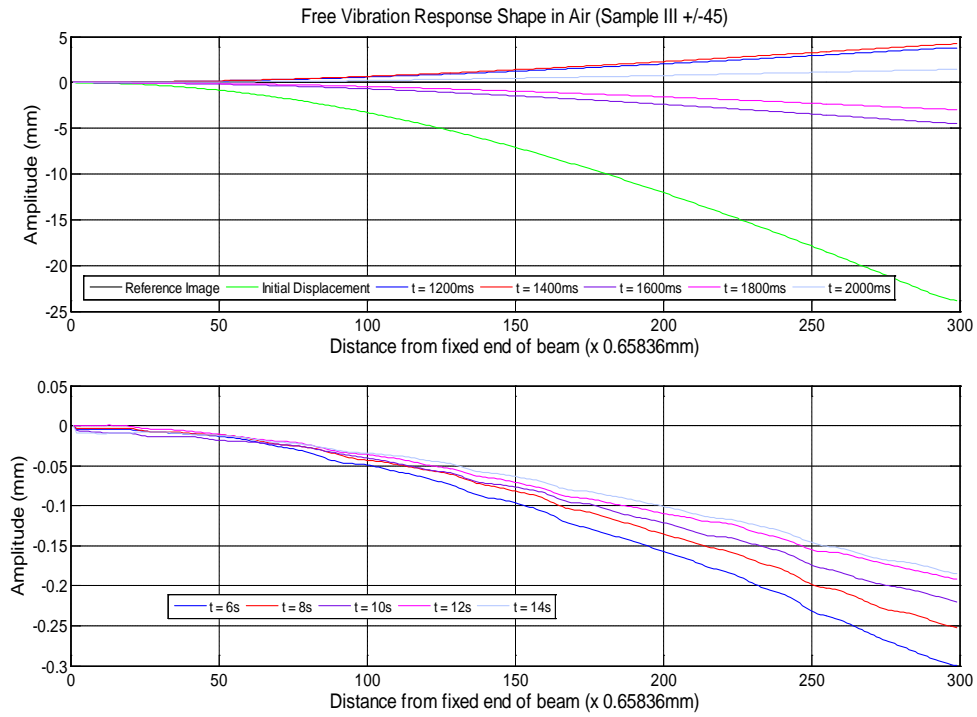


Figure 54. Free vibration response shape in air at various times for Sample III of $\pm 45^\circ$ orientation

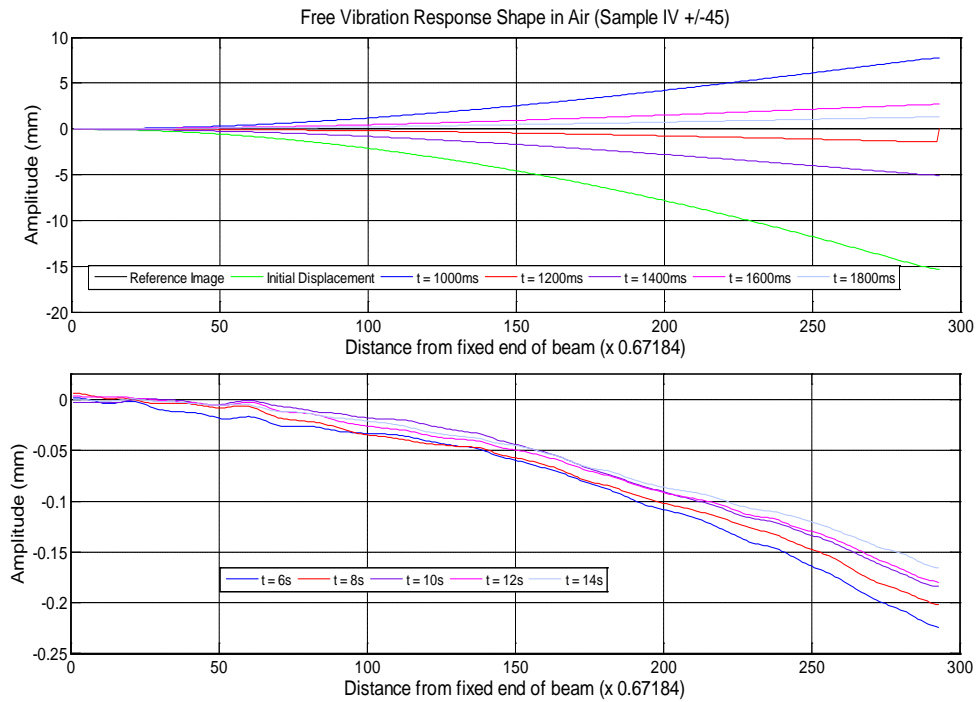


Figure 55. Free vibration response shape in air at various times for Sample IV of $\pm 45^\circ$ orientation

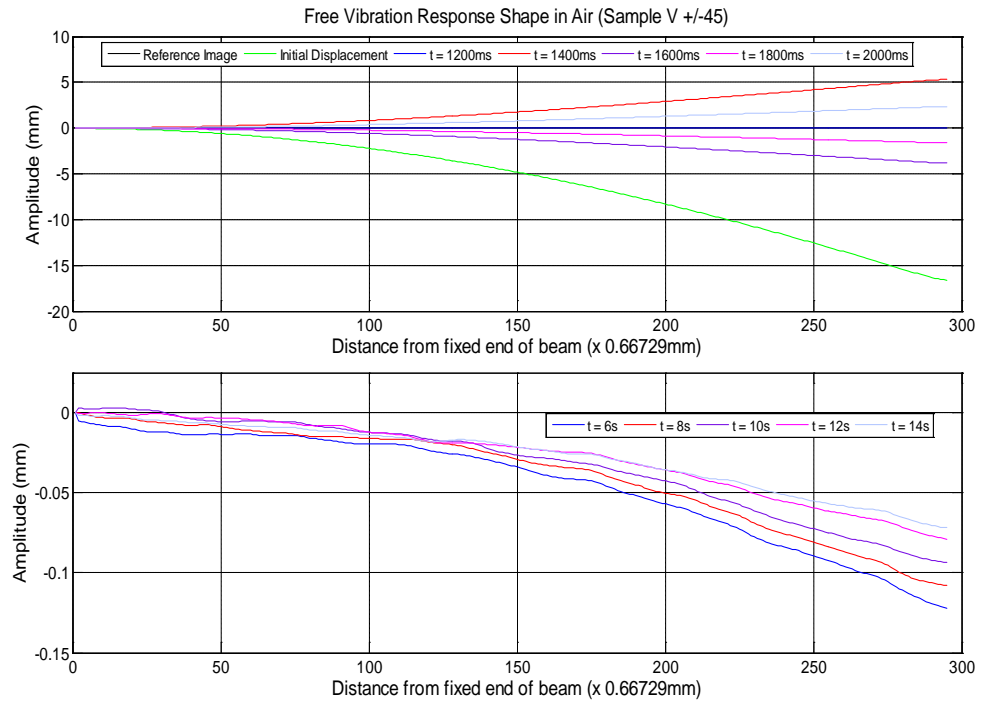


Figure 56. Free vibration response shape in air at various times for Sample V of $\pm 45^\circ$ orientation

APPENDIX C: FREE VIBRATION RESPONSE IN WATER PLOTS

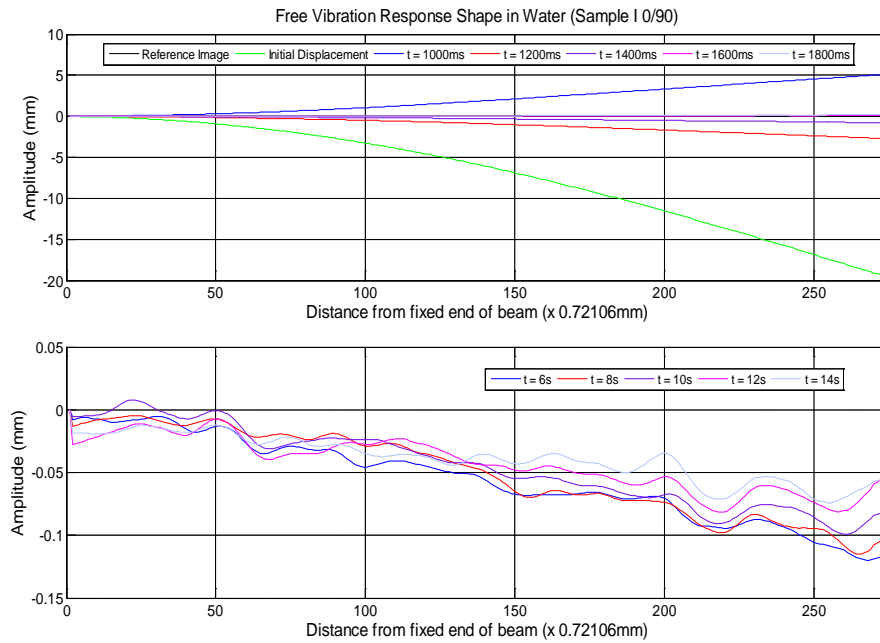


Figure 57. Free vibration response shape in water at various times for Sample I of $0^\circ/90^\circ$ orientation

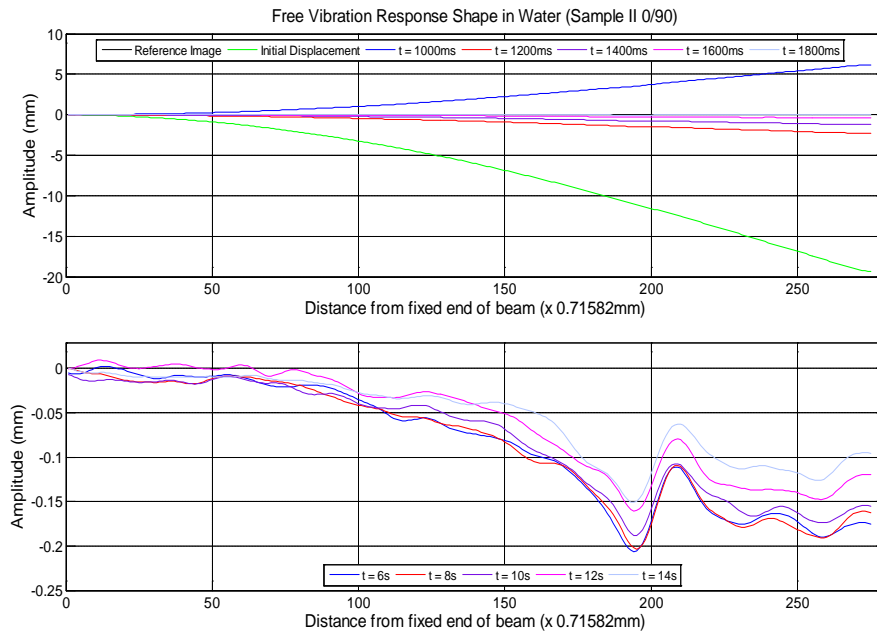


Figure 58. Free vibration response shape in water at various times for Sample II of $0^\circ/90^\circ$ orientation

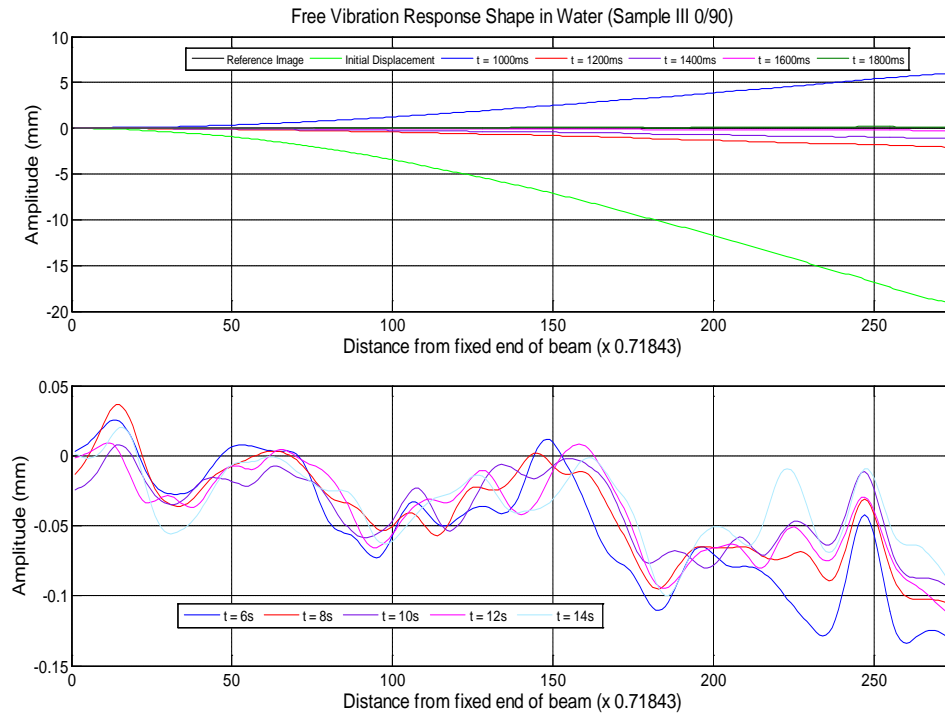


Figure 59. Free vibration response shape in water at various times for Sample III of $0^\circ/90^\circ$ orientation

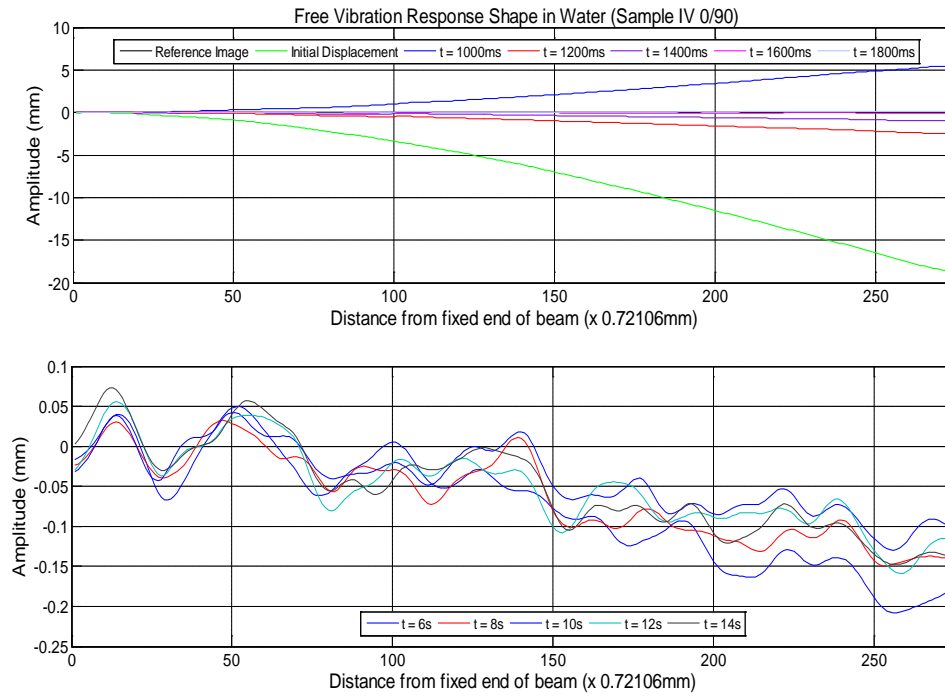


Figure 60. Free vibration response shape in water at various times for Sample IV of $0^\circ/90^\circ$ orientation

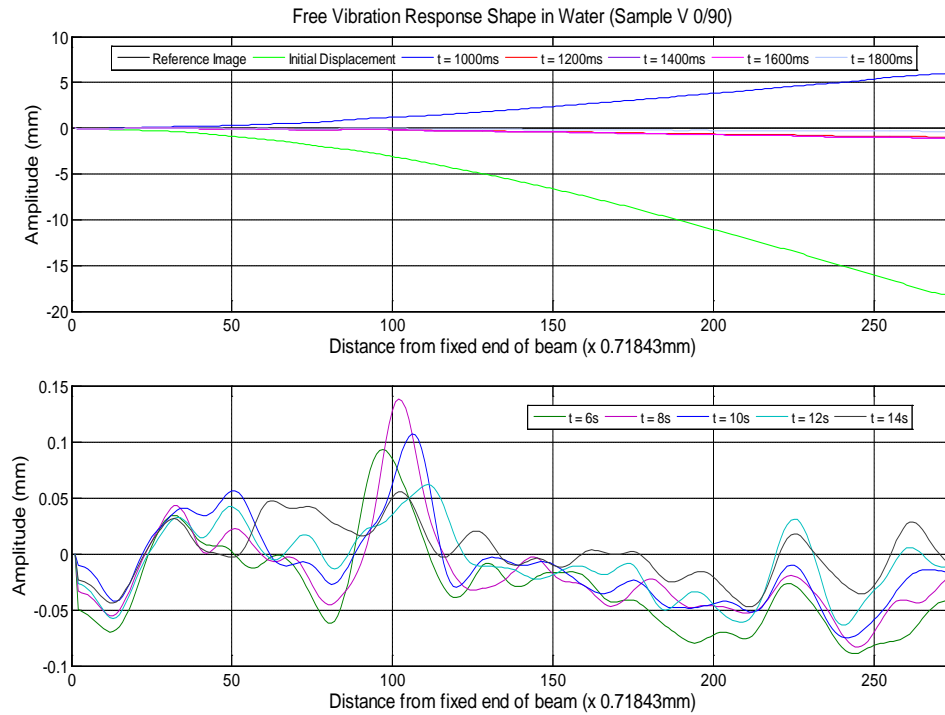


Figure 61. Free vibration response shape in water at various times for Sample V of $0^\circ/90^\circ$ orientation

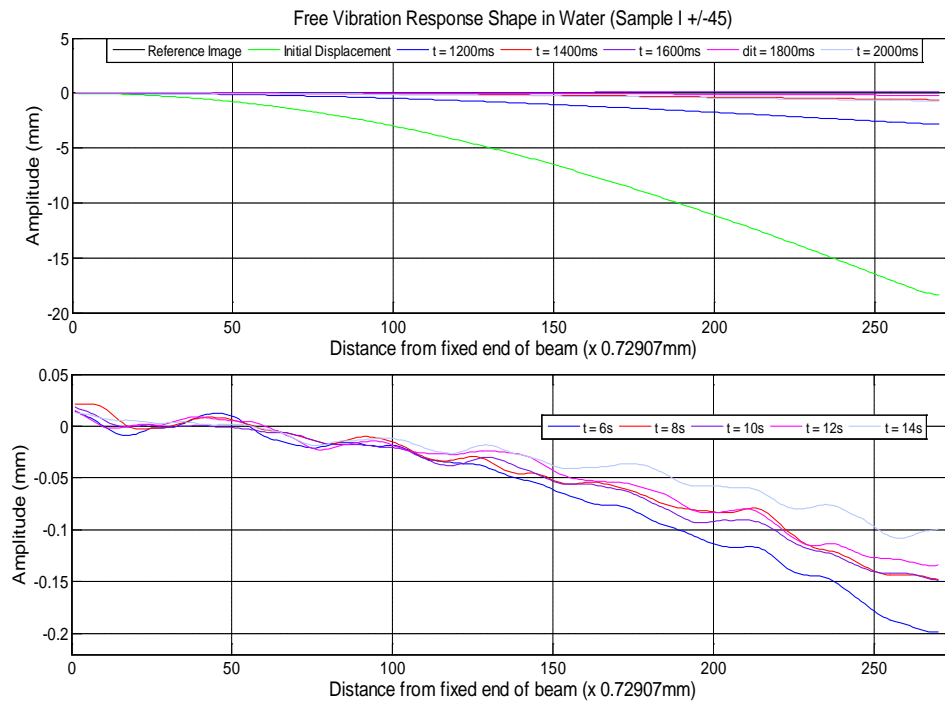


Figure 62. Free vibration response shape in water at various times for Sample I of $\pm 45^\circ$ orientation

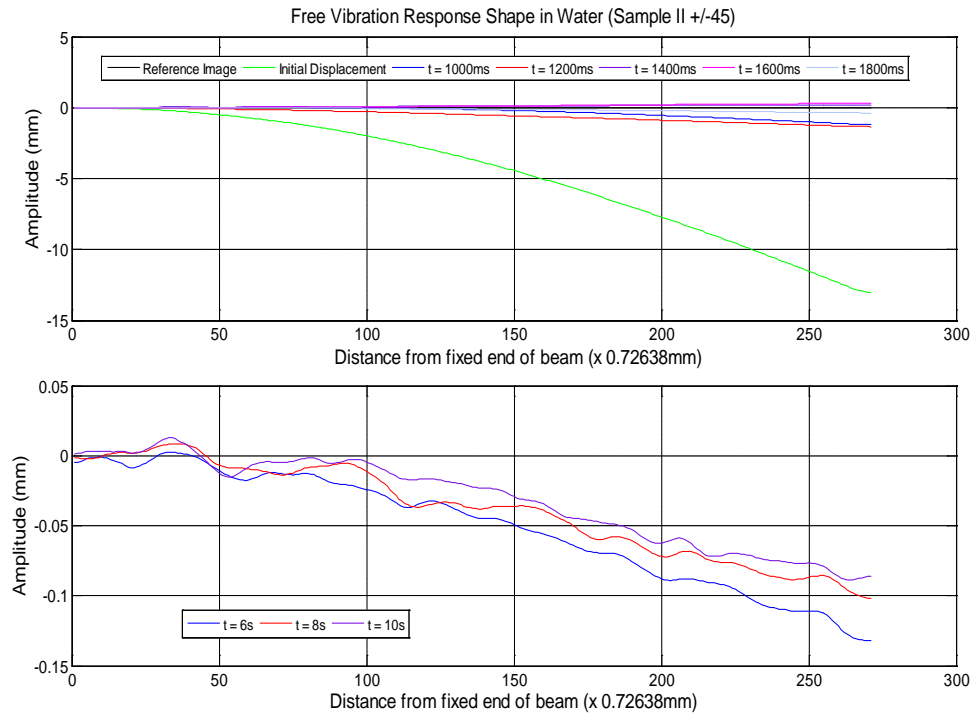


Figure 63. Free vibration response shape in water at various times for Sample II of $\pm 45^\circ$ orientation

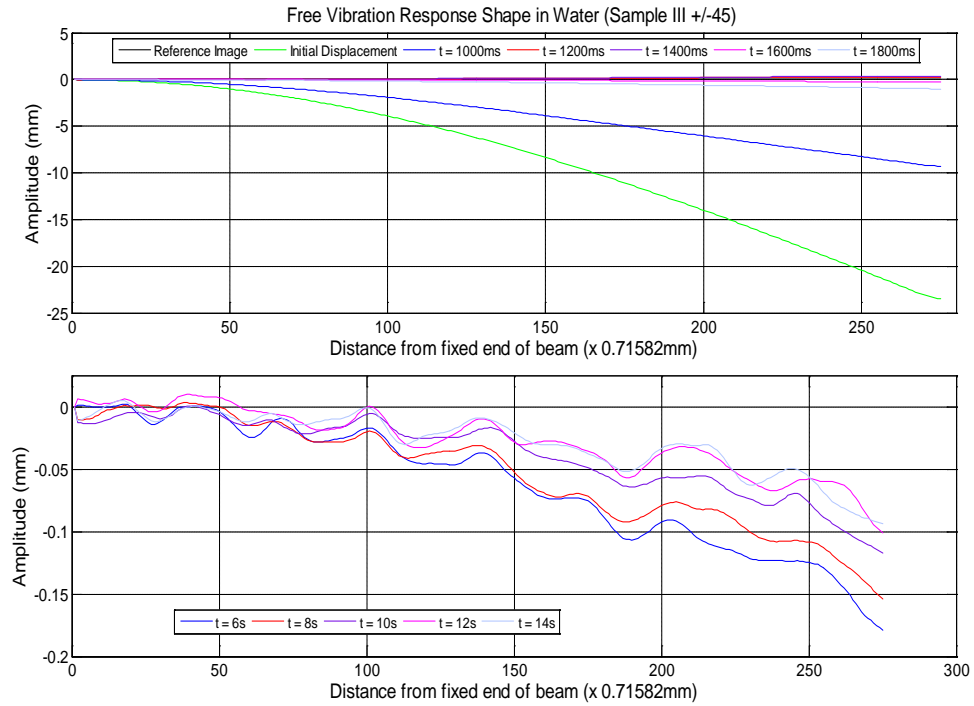


Figure 64. Free vibration response shape in water at various times for Sample III of $\pm 45^\circ$ orientation

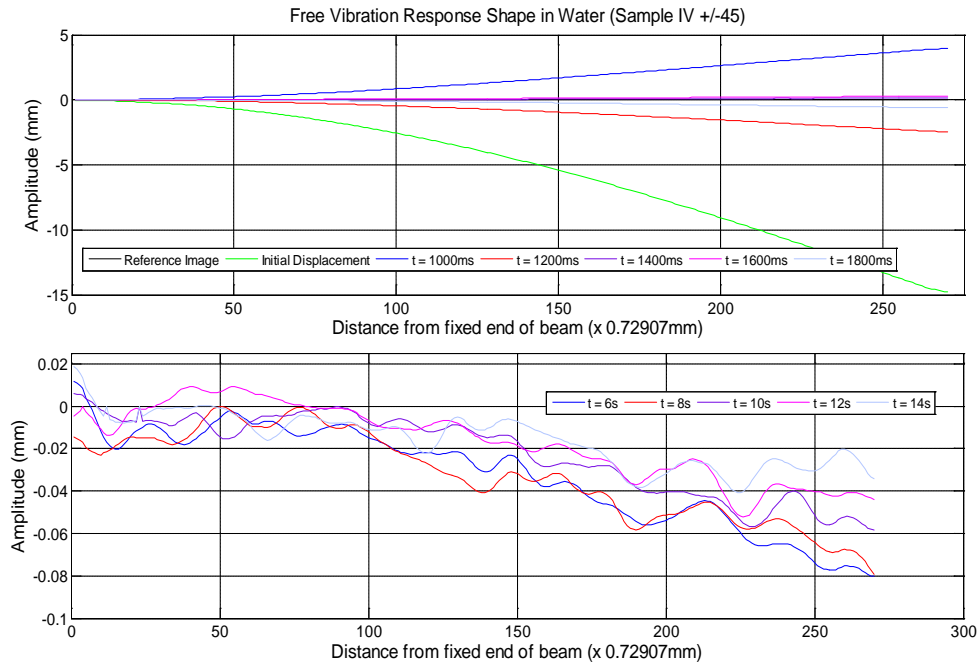


Figure 65. Free vibration response shape in water at various times for Sample IV of $\pm 45^\circ$ orientation

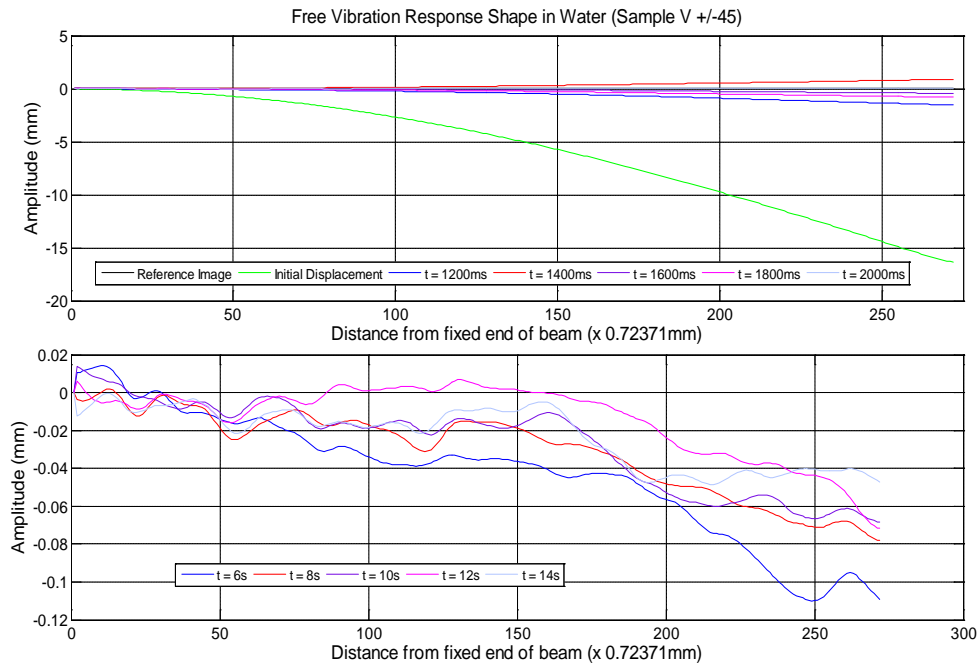


Figure 66. Free vibration response shape in water at various times for Sample V of $\pm 45^\circ$ orientation

THIS PAGE INTENTIONALLY LEFT BLANK

LIST OF REFERENCES

- [1] P. Noury and B. Hayman, "Lightweight construction for advanced shipbuilding—recent development," *Det Norske Veritas*, pp. 1–23, 2002.
- [2] R. Schwarting et al. "Manufacturing techniques and process challenged with CG47 class ship aluminum superstructures modernization and repairs," in *Fleet Maintenance & Modernization Symposium 2001: Assessing Current & Future Maintenance Strategies*, San Diego, 2011.
- [3] E. Cormack, "The Effect of Sensitization on the Stress Corrosion Cracking of Aluminum Alloy 5456," Naval Postgraduate School, 2012.
- [4] P. Koenig, "Ship service life and naval force structure," *Naval Engineers Journal*, vol. 121, no. 1, pp. 69–77, 2009.
- [5] L. H. Strait, M.L. Karasek, and M. F. Amateau, "Effects of Stacking Sequence on the Impact Resistance of Carbon Fiber Reinforced Thermoplastic Toughened Epoxy Laminates," *Journal of Composite Materials*, vol. 26, no. 12, 1992, pp. 1725–1740.
- [6] M. O. W. Richardson and M. J. Wisheart, "Review of Low-Velocity Impact Properties of Composite Materials," *Composite Part A*, vol. 27A, pp. 1123–1131, 1996.
- [7] A. Owens, "An Experimental Study of Fluid Structure Interaction of Carbon Composites Under Low Velocity Impact," Naval Postgraduate School, 2009.
- [8] R. McCrillis, "Dynamic Failure of Sandwich Beams With Fluid-Structure Interaction Under Impact Loading," Naval Postgraduate School, 2010.
- [9] R. Conner, "Fluid Structure Interaction Effects on Composites Under Low Velocity Impact," Naval Postgraduate School, 2012.
- [10] M. K. Kwak, K. C. Kim, "Axisymmetric vibration of circular plates in contact with fluid," *Journal of Sound and Vibration*, vol 146, pp 381–389, 1991.
- [11] M. K. Kwak, "Hydroelastic vibration of rectangular plates," *Journal of Applied Mechanics*, vol 63, pp 110–115, 1996.
- [12] I. Correlated Solutions, "Digital Image Correlation□: Overview of Principles and Software." pp. 1–101, 2009.

- [13] H. Lu and P. Cary, "Deformation measurements by digital image correlation: Implementation of a second-order displacement gradient," *Experimental Mechanics*, vol. 40, no. 4, pp. 393–400.
- [14] R. Student and R. Cintrón, "Strain measurements with the digital image correlation system vic-2D," *System*, no. September, 2008.
- [15] L. PI and L. Smith, "Measure Strain Distribution Using Digital Image Correlation (DIC) for Tensile Tests," 2010.
- [16] H. Yuanhao, "Development of digital image correlation method for displacement and shape measurement," no. June, 2004.
- [17] Hewlett-Packard, "Application Note 243-3: The Fundamentals of Modal Testing," 1986.
- [18] D. E. LLC, "A beginner's guide to accelerometers." [Online]. Available: <http://www.dimensionengineering.com/info/accelerometers>.
- [19] LDS-Dactron, "Application Note AN011: Basics of Structural Vibration Testing and Analysis," 2003.
- [20] Y. W. Kwon and H. Bang, *The Finite Element Method Using MATLAB*, 2nd Ed. New York: CRC Press LLC, 2000, pp. 237–306.
- [21] Ridout Plastics Co. Inc, (2012). *Weld-on #40 Pint Kit (A+B) Plexiglass Glue Adhesive* [Online]. Available: http://www.eoplastics.com/Plastic/Lexan_Polycarbonate_Glue/PLEXIGLASS-GLUE-ADHESIVE-IPS40-PT
- [22] H. E. Ross et al. "Adaptation of divers to size distortion under water," *Br. J. Psychology*, 61, pp. 365-373, 1970.
- [23] Ashland Inc, (2012). *Derakane epoxy vinyl ester resin* [Online]. Available: <http://www.ashland.com/products/derakane-epoxy-vinyl-ester-resin>
- [24] M. Simonsen, "CSI Application Note AN-722," 6 April 2011. [Online]. Available: <http://www.correlatedsolutions.com/installs/Vic-3D-2010-manual.pdf>.

INITIAL DISTRIBUTION LIST

1. Defense Technical Information Center
Ft. Belvoir, Virginia
2. Dudley Knox Library
Naval Postgraduate School
Monterey, California
3. Professor Young W. Kwon
Naval Postgraduate School
Monterey, California
4. Professor Joshua H. Gordis
Naval Postgraduate School
Monterey, California
5. Research Assistant Professor Jarema M. Didoszak
Naval Postgraduate School
Monterey, California
6. Eric M. Priest
Naval Postgraduate School
Monterey, California